THE ELECTROMAGNETIC SIMULATION OF BIRDCAGE COILS FOR MRI BASED ON FINITE ELEMENT METHOD

by

Yonatan Tadesse

Submitted in Partial Fulfillment of the Requirements

for the Degree of

Master of Science

in the

Electrical Engineering

Program

YOUNGSTOWN STATE UNIVERSITY

FALL 2016

THE ELECTROMAGNETIC SIMULATION OF BIRDCAGE COILS FOR MRI BASED ON FINITE ELEMENT METHOD

Yonatan Tadesse

I hereby release this thesis to the public. I understand that this thesis will be made available from the OhioLINK ETD Center and the Maag Library Circulation Desk for public access. I also authorize the University or other individuals to make copies of this thesis as needed for scholarly research.

Signature:

Yonatan Tadesse, Student Date

Approvals:

Dr. Lin Sun, Thesis Advisor Date

Dr. Philip C. Munro, Committee Member Date

Dr. Frank Li, Committee Member Date

Dr. Salvatore A. Sanders, Dean of Graduate Studies Date

Abstract

Radio frequency birdcage coils are widely used in clinical magnetic resonance imaging. In order to effectively design a birdcage coil, optimum capacitance calculation on the rungs or end rings is critical. Several methods are discussed in this thesis to calculate the capacitance. The first method is called lumped circuit element method, which is a commonly used technique to calculate the capacitance and resonant modes. However, the RF coil design begins to fail under quasi-static assumption as the frequency increases. Therefore, to accurately determine the capacitance, we use frequency domain analysis method for both the low-pass and high-pass birdcage coils in COMSOL Multiphysics. Modeling the birdcage coil in a 3D simulation environment helps to analyze the electromagnetic field and absorbed power in the volume of interest, such as field homogeneity, circularity, and specific absorption rate (SAR). In order to verify the optimal capacitance value, a computer program (Birdcage Builder) is used based on the model designed. Four frequencies are considered for the simulation, 64 MHz, 127.5 MHz, 170 MHz and 200 MHz corresponding to 1.5 T, 3 T, 4 T and 4.7 T MRI systems respectively.

Acknowledgment

First and foremost, I would like to thank my lord and savior Jesus Christ for making all things possible. Second, I would like to express my greatest gratitude to my advisor Dr. Sun for her encouragement and endless hours helping me throughout my thesis work. It is without a doubt, I would not able to do it without her assistance and guidance.

I would also like to thank Dr. Munro and Dr. Li for taking the time to be my committee members to review and attend my thesis defense. I am also thankful to Dr. Jalali for his valuable advice and help throughout my 6 years at Youngstown State University. I would also like to thank Dr. Hui Xie at Houston Formation Evaluation Center, Schlumberger at Sugar Land, TX for giving his valuable comments on my thesis.

Last but not least, I would like to thank my family and girlfriend for motivating me and being my moral support through my ups and downs. I will not pass without acknowledging the sacrifices my parents have made for me to study in the United States. Therefore, I would like to take this opportunity to thank them and tell them their time and money did not go to waste.

Table of Contents

List of Figures

List of Tables

CHAPTER 1

INTRODUCTION

1.1. Magnetic Resonance Imaging

Magnetic Resonance Imaging (MRI) is a powerful medical diagnostic technique based on nuclear magnetic resonance (NMR) which is used in medicine to conduct different treatments including cardiovascular and neurological imaging, cancer, genetic and metabolic diseases, infections and inflammatory conditions, traumatic and other types of injuries. The primary source of MRI signal comes from Hydrogen nucleus (positive electrical charge) because of its abundance in water (H_2O) and fat. The protons in the hydrogen nuclei constantly spin and have their own magnetic field as the result of the moving electric charge. At room temperature and with no external magnetic field (B_0), the magnetic moment of each proton in the human body is randomly oriented. However, when an external magnetic field (B_0) is applied in the z direction, the hydrogen molecules align either parallel or anti-parallel to the external field. The proton may either assume the low energy orientation with the z-component of its magnetic moment aligned with the external magnetic field called the 'parallel state' or with the z-component of its magnetic moment aligned opposite to the external field called the 'anti-parallel state' [1]. The energy associated with the parallel state is lower than that of the anti-parallel state as shown in Figure 1.

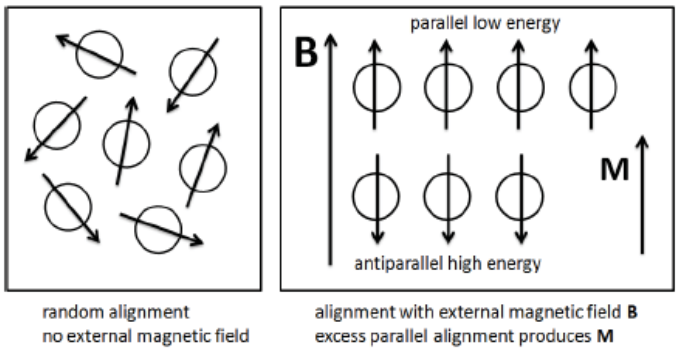

Figure 1: Hydrogen nuclei before and after external magnetic field (Image from Westbrook [2])

1.2 Precession

When put in the external magnetic field, the individually aligned parallel or anti-parallel protons spin in a particular way called precession. The speed of the precession is how many times the protons precess per second and is determined by the Larmor equation.

$$\omega = \gamma B_0 \tag{1.1}$$

where ω is called the Larmor frequency in rad/sec. The gyromagnetic ratio (γ) for Hydrogen molecule has a constant value of 42.6 MHz/Tesla. Figure 2 shows the classical example of spinning top about the Earths gravitation field **G** versus hydrogen nucleus.

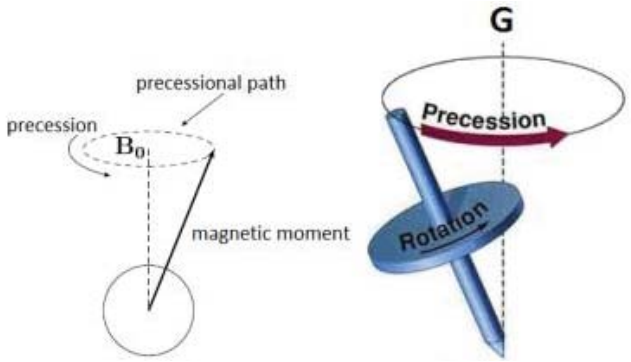

Figure 2: Precession of hydrogen nucleus compared to a classical spinning top (Image from Westbrook [2])

1.3 Longitudinal and Transverse Magnetization

Opposing protons neutralize each other leaving a net number of protons parallel to B_0 in the z-axis. The sum magnetization is parallel to the external magnetic field and called longitudinal magnetization. Inside MRI, the patient acts as a bar magnet aligned with B_0 which makes it impossible to measure the magnetic field of the patient as it is in the same direction as the external magnetic field.

The purpose of radio frequency (RF) pulse is to distort the protons so they fall out of alignment with the external magnetic field (B_0). This only happens if the RF pulse has the same precessional frequency, which is called resonance. Thus, this magnetic resonance is set at the Larmor frequency. The RF field is also responsible for the spin tipping produced by the RF coil, which will be discussed in Chapter 2. The tip

angle θ depends on the B_1 field, a time varying excitation perpendicular to the static magnetic field as well as its duration t as described in Eq. (1.2). The tipping of the magnetization can be seen from the rotating frame *M* itself as shown in Figure 3.

$$\theta = \gamma B_1 t \tag{1.2}$$

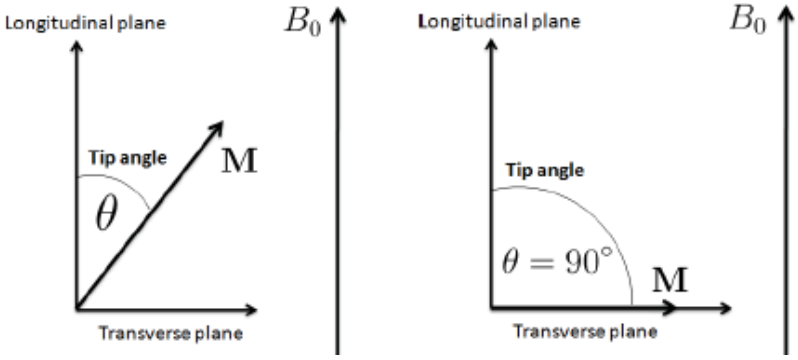

Figure 3: Flip angle of the magnetization *M* in the rotating frame of reference (Image from Westbrook [2])

Two major effects happen during the activation of the RF pulse. First, some of the protons gain energy from the RF pulse and fall into the higher energy state, resulting in the reduction of longitudinal magnetization. Second, the RF pulse pushes the protons to synchronize in phase with each other instead of in random direction. This result is called transverse magnetization in which the net magnetization is the *x*-*y* plane with the precessing protons at the Larmor frequency.

Transverse magnetization is a moving magnetic field at Larmor frequency and if a receiver coil or antenna is placed near, an alternating voltage will be induced which generates electrical current. This current can be picked up to form MR signal. Immediately after the RF pulse is switched off, the protons start to fall out of phase and return to the lower energy state called relaxation.

Relaxation occurs in two forms, T_1 and T_2 relaxation. T_1 occurs when the longitudinal magnetization return to its original value [1] while T_2 relaxation is the disappearance of the transverse magnetization.

1.4 T_1 Relaxation

The application of a resonant RF pulse disrupts the spin system; however, there is a process that makes it come back to equilibrium. T_1 relaxation also called spin-lattice relaxation is a process by which protons exchange energy with their surroundings to return to their lower energy state restoring longitudinal magnetization. At equilibrium the net magnetization M_0 is parallel to the magnetic field B_0. The z-component of the magnetization M_z (i.e. longitudinal magnetization) can be saturated to zero by exposing it to the energy at a frequency equal to the energy difference between the two spin states. The spin-lattice relaxation (T_1) describes how M_z can return to its equilibrium values.

$$\frac{dM_z}{dt} = \frac{M_z - M_0}{T_1} \tag{1.3}$$

$$M_z = M_0\ (1 - e^{-t/T_1})$$

As seen in Figure 4, the spin-lattice is the relaxation time to reduce the difference between the longitudinal magnetization (M_z) and it's equilibrium by a factor of e [3].

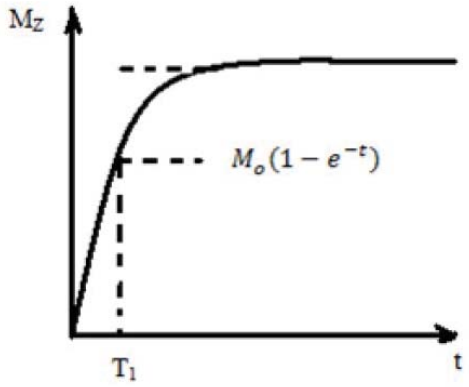

Figure 4: T_1 Processes

1.5 T_2 Relaxation

T_2 relaxation, also called spin-spin relaxation, describes how the protons fall out of phase in the *x-y* plane. There are two main causes for this loss of phase. The first, T_2 relaxation, results from a slowly fluctuating magnetic field with neighboring nuclei. This results in the random fluctuation of the Larmor frequency of individual protons causing

an exchange of energy between proton spins, which leads to loss of phase coherence across a population of protons [2]. The second cause of phase is inhomogeneity of static magnetic field B_0 causing slightly different Larmor frequencies for protons at different locations. T_2 (spin-spin relaxation time) is a constant describing the time taken for the transverse magnetization, M_{xy} to decay. The net magnetization in the *x*-*y* plane goes to zero, and the longitudinal magnetization grows until we have M_0 along *z* [3].

$$\frac{dM_x}{dt} = -\frac{M_x}{T_2} \; ; \; \frac{dM_y}{dt} = -\frac{M_y}{T_2} \tag{1.4}$$

$$M_{xy}(t) = M_{xy}\, e^{-t/T_2}$$

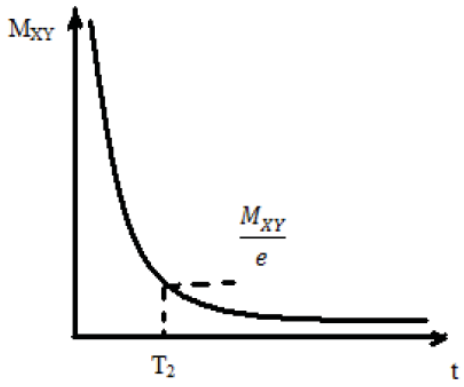

Figure 5: T_2 Processes

Since T_2 relaxation (spin-spin relaxation) is solely the interaction between the spins, there is no transfer of energy (dissipation of energy) to the surrounding tissues. However, as mentioned in section 1.4, when the protons return back their original state (lower energy state); they dissipate energy in the form of heat to the surrounding tissues.

1.6 Static Magnetic Field

As briefly mentioned in the introduction section, static magnetic field is used to align the hydrogen nuclei when the patient is placed inside MRI. There are three ways to generate this field, fixed magnets, resistive magnets and super-conductive magnets. Fixed magnets and resistive magnets are restricted to field strength of below 0.4 T. Therefore, these types of magnets are not recommended since high field strength is required to get high resolution quality imaging. The super-conducting magnets on the

contrary are used in modern MRI scanning systems as they able to produce highly uniform and stable magnetic field [4].

The Superconducting magnet used in MRI is an electromagnet made from coils of superconductive wire. These coils of wires at their superconducting state can conduct electricity than ordinary wire to produce strong magnetic field. The coils are soaked in liquid helium below cryogenic temperature to reduce rise in temperature.

1.7 Gradient Coils

Gradients are loops of wires on a cylindrical shell inside the bore of the primary magnet. When current passes through these coils a secondary magnetic field is generated. The secondary magnetic field is used to alter the strength of the main magnetic field causing the resonance frequency of the proton to vary as a function of position. Therefore, the resonant frequencies of the hydrogen nuclei are spatially dependent within the gradient. Different areas in the body can be stimulated by exciting the coil at different frequencies.

All MRI systems have three sets of gradients coils, *x*, *y* and *z*. The coils are arranged opposite to each other to produce North and South Pole to provide slice selection. The arrangement of these coils gives MRI the capacity to image directionally along each axis. The *z* gradient runs along the long axis to produce axial images while the *y* gradient runs along the vertical axis to produce coronal images and the *x* gradient runs along the horizontal axis to produce sagittal images. In the remainder MRI experiment, the *y* gradient performs "Phase Encoding" while the *x* gradient performs the "Read Out". The x and y gradients are switched on and off during a pulse sequence in order to fill out the *k*-space. Figure 6 shows a standard MRI scanner with three types of coils [5].

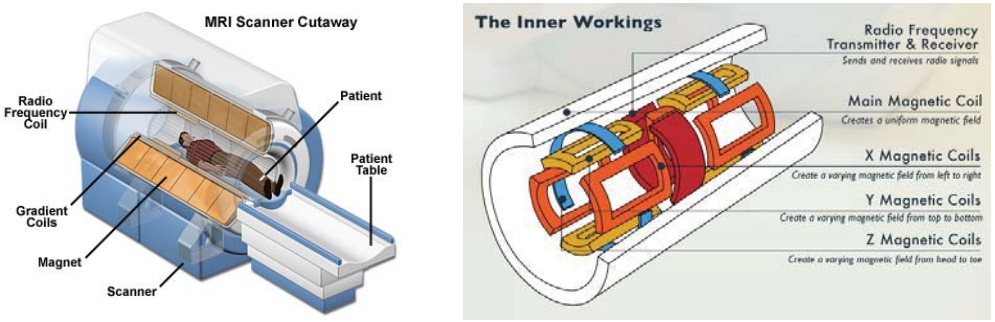

Figure 6: MRI scanner

CHAPTER 2

RADIO FREQUENCY COILS

INTRODUCTION

Radio Frequency coils are essential elements in Magnetic Resonance Imaging. According to their functions, they can be divided in three groups: transmit only, receive only and transmit/receive coils. As a transmitter, RF coil generates rotating magnetic field (B_1) perpendicular to the static magnetic field (B_0). This rotating field excites the nuclei (spins) in the object at the Larmor frequency. Providing good homogeneity, transmit coils are highly recommended, i.e. birdcage coils and transverse electromagnetic coils can be used as transmit coils. As a receiver, the coil picks up the RF electromagnetic radiation produced by nuclear relaxation inside the object as the nuclei recover. Although RF coils may serve as both transmitter/receiver (T/R), today's modern scanners utilize separate T/R systems.

Fields between 1.5 T to 4 T exhibit good signal to noise ratio, transverse B_1 field uniformity and low specific absorption rate (SAR) in the biological tissues. However, for high field (>4 T) MRI systems, RF coils face major difficulties. Increasing the Larmor frequency increases the static magnetic field linearly which causes the operational wavelength to decrease. At high frequencies, the interaction between the B_1 field and the human body can no longer be neglected. This interaction is caused by the dielectric resonance, since the effective wavelength of the B_1 field is now compatible or even smaller than the dimension of the human body [6]. Such interaction can lead to inhomogeneity of the B_1 field, nonuniform current distribution on the RF coil struts and high SAR causing damages to sensitive parts of the body such as the brain and eye.

In this thesis, birdcage coil, one of the most used RF coils is discussed in detail. The following chapters will emphasize on the design and simulation of low-pass and high-pass birdcage coils between 1.5 T – 4.7 T.

2.1 RF Birdcage Coils

RF birdcage coils have become widespread in the field of MRI imaging. Their simplicity in design followed by a high homogenous magnetic field due to continuous sinusoidal current distribution on the surface of the coil led to their popularity. The birdcage coil is the mostly used RF transmit device in clinical MRI. Throughout the years researchers have fine-tuned birdcage coils by increasing the length of the rungs, employing RF shields, four-port drive and various methods to increase the sensitivity of the coil to get good B_1 field homogeneity. In order to study magnetic field homogeneity, linear, quadrature and four-port excitation are used for different coil loading. In addition, birdcage coils can be used for quadrature excitation and reception that provide better power efficiency in transmit mode and higher MR signal sensitivity in receive mode compared to linear excitation and reception [6].

RF birdcage coil consists of two circular loops referred as end rings connected by equally spaced even number of straight elements, which are called rungs or legs. The important feature of the circular birdcage coil is that the homogenous field inside the coil can be achieved by soldering equal value capacitors on the coil [7]. Often a birdcage resonator with higher number of legs is desired for improved RF field homogeneity [8]. In clinical MRI, according to the location of the capacitor on the coil geometry, three kinds of configurations are used, low-pass, high-pass and band-pass birdcage resonator as shown in Figure 7.

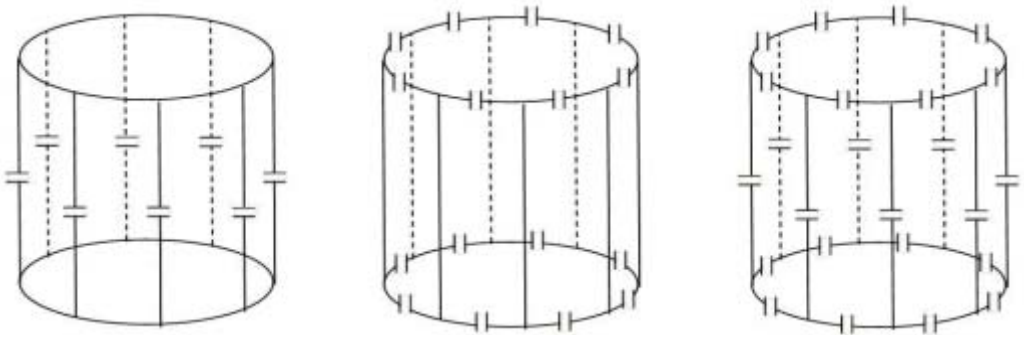

(a) (b) (c)

Figure 7: Models of birdcage coils (a) low-pass (b) high-pass (c) band-pass coil

As shown in Figure 7, a low-pass coil has capacitors placed on the legs, while high-pass coil has distributed capacitors placed on the end ring segments. A band-pass coil has capacitors at both locations (legs and end-rings). A birdcage coil with *N* number of legs and equal valued capacitors has *N/2* distinct resonant modes, when the mode number $m = 1$, it is the lowest frequency resonant for low-pass and highest frequency for high-pass birdcage coil. This can generate a sinusoidal current distribution in the rungs resulting homogeneous B_1 field inside the coil. Resonant modes, $m = 1, 2, 3..., (\frac{N}{2})$, are also called degenerate mode pairs which are actually two modes having the same resonant frequency but represented with the same m and produce B_1 field that are perpendicular to each other [10]. Quadrature excitation uses these two orthogonal modes to produce B_1 fields that are perpendicular to each other. A birdcage coil can be driven from two ports that are geometrically 90^o apart with phase difference 90^o as shown in Figure 8. By driving the coil in this manner, it will generate a circularly polarized B_1 field of the form

$$\boldsymbol{B_1} = B_1\,(\cos(\omega t)\,\hat{x} + \sin(\omega t)\,\hat{y}) \tag{2.1}$$

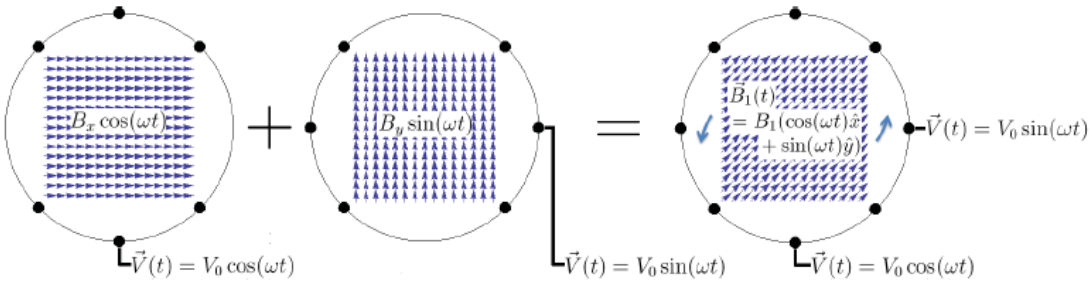

Figure 8: Axial view of birdcage coil using quadrature excitation

2.2 Lumped Circuit Element Analysis

A lumped circuit element method is widely used in the modeling of birdcage coils. In this method, the rungs and end rings are first modeled as inductors. Then self and mutual inductances of these elements are calculated using handbook formulas [9]. The equivalent circuit is solved by using Kirchhoff's voltage and current laws.

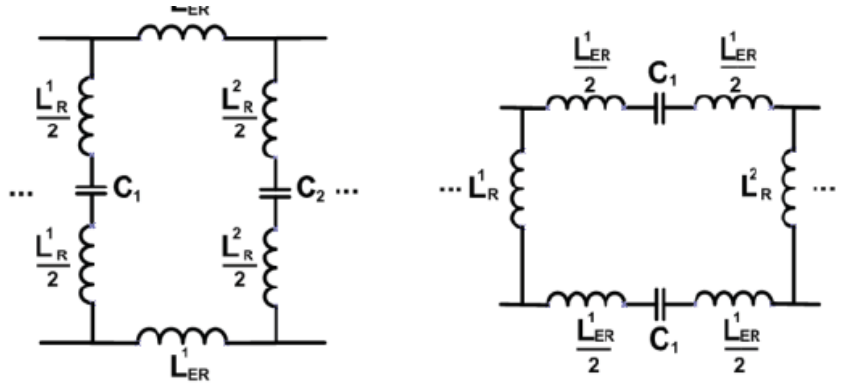

Figure 9: Lumped circuit element models (a) low-pass coil (b) high-pass coil

Equivalent lumped circuits for one closed loop of a low-pass and a high-pass birdcage coil are illustrated in Figure 9. Only high-pass and low-pass birdcage coils are considered [8].

Since the calculation to determine the self and mutual inductance of the coil elements are made under the quasi-static assumption, errors in the calculations of capacitance and resonant modes increase as the resonance frequency increases to a point where the wavelength is in the order of the coil dimensions. There is an important criterion, which is used for determining whether a wire can be modeled as lumped circuit element or not [10]. That is,

$$\text{Length of wire} \leq \frac{\lambda}{20}$$

where λ is the wavelength and any wire longer than one twentieth of the wavelength will give defective results. Therefore, this method can be used in design of birdcage coil at low frequencies only.

It is difficult and time-consuming to analyze and calculate RF coils due to the complexity of their structure based on Maxwell's equations. However, by making the coil size fraction of the wavelength, we can analyze using equivalent circuit method.

Let's consider a simple surface RF coil made of circular copper wire with a capacitor. By modeling the wire as inductor, the coil can be represented as equivalent circuit seen in Figure 10.

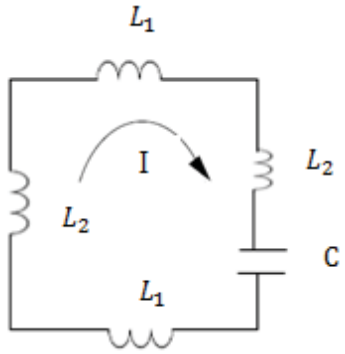

Figure 10: Equivalent circuit of a simple RF coil

The self-inductance of the coil can be calculated using the coil's radius and length from the formula given as

$$L = 0.02l\left[\ln\left(\frac{2l}{a}\right) - 1)\right] \tag{2.2}$$

where l is the length and a is the radius of the circular wire.

Using Kirchhoff's voltage law, the equivalent circuit can be analyzed as given

$$\frac{i}{\omega C}I - 2i\omega L_1 I + 2i\omega M_1 I + 2i\omega L_2 I + 2i\omega M_2 I = 0 \tag{2.3}$$

where M_1 is the mutual inductance between the horizontal wires, while M_2 is between the two vertical wires. For two perpendicular wires, $M_{12} = M_{21} = 0$. However, for two parallel wires having the same length and distance to each other, the mutual inductance becomes [11]

$$M = 0.002l\left[\left(\frac{l}{d} + \sqrt{\frac{l^2}{d^2}}\right) - \sqrt{1 + \frac{d^2}{l^2}} + \frac{d}{l}\right] \tag{2.4}$$

where *d* is the distance between the two wires, *l* is the length of the wire. From Eq. 2.3, we can find the resonant frequency as

$$\omega_r = \frac{1}{\sqrt{2(L_1+L_2-M_1-M_2)C}} \tag{2.5}$$

2.3 Low-pass Birdcage Coil

The simple surface RF coil equivalent circuit analysis can be extended to design more complicated coils. One of the most common RF coils used in MRI is the birdcage coil. Let's consider low-pass birdcage coil as shown in Figure 11 [12]. Low-pass birdcage coil consists of two end rings connected by equally spaced *N* number of legs (rungs), each containing a capacitance between the legs.

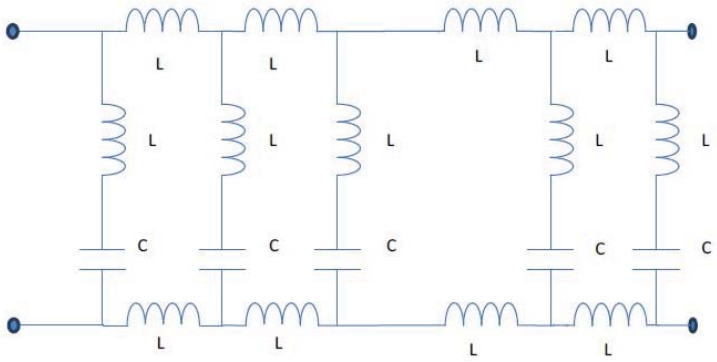

Figure 11: Lumped element equivalent circuit of a low-pass birdcage coil

The inductors in the rungs are coupled by mutual inductance while the inductors at the end rings are coupled by inductive coupling. The resonant phenomena can be understood by considering wave propagation in a periodic structure [13]. Each of the N repeated element introduces a phase shift transmission $\Delta\Phi(\omega)$. The total phase shift must be an integer of 2π. Hence, the resonant condition is $N\Delta\Phi(\omega)= 2\pi m$. Derivation of $\Delta\Phi(\omega)$ is possible by neglecting the mutual inductance and by setting $C_1 = C_2 = \ldots = C$, $L_1 = L_2 = \cdots = L$ and $M_{11} = M_{22} = \ldots = M$.

The simplified network is a low-pass filter with a spectrum of $N/2$ resonance at frequency given by

$$\omega_r = \frac{2}{\sqrt{LC}} \sin\left(\frac{\pi m}{N}\right) \tag{2.6}$$

where $l \leq m \leq N/2.$

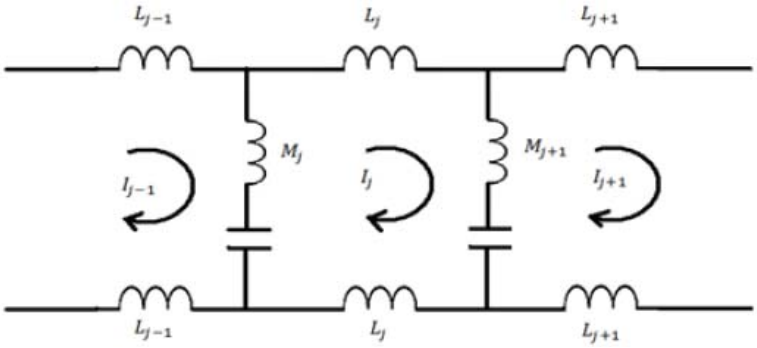

Figure 12: Current distribution of a low-pass birdcage coil

A standing wave in low-frequency mode (m = 1) generates current in the straight segments proportional to sin θ producing homogenous B_1 field inside the cylinder. For $m = N/2$, adjacent segments have equal current in magnitude but different in direction.

Applying Kirchhoff's voltage law we can solve Figure 12, we obtain

$$\left(\frac{1}{\omega^2 C} - M\right)\left(I_{j+1} + I_{j-1}\right) - 2\left(\frac{1}{\omega^2 C} - L - M\right) I_j = 0, \; j = 1, 2\ldots, N \quad (2.7)$$

Because of cylindrical symmetry, the current I_j must satisfy the periodic condition $I_{j+N} = I_j$. Therefore, N is linear independent solution (or modes) have the form

$$I_j = \cos\frac{2\pi m j}{N}, \; m = 0, 1, 2,\ldots, N/2 \quad (2.8)$$

$$I_j = \sin\frac{2\pi m j}{N}, \; m = 0, 1, 2,\ldots, N/2 - 1$$

where I_{jm} is the value of the current in the j^{th} leg of the m^{th}solution. The current distribution in low-pass birdcage coil [7, 14, 15] is shown in Figure 12.

The resonant frequency can be found by substituting Eq. 2.8 into Eq. 2.7 and the result is found to be

$$\omega_m = \left[C\left(M + \frac{L}{2}\sin^2\frac{\pi m}{N}\right)\right]^{-1/2}, \; m = 0, 1, 2,\ldots, N/2 \quad (2.9)$$

The end ring mode at $m = 0$ is the lowest resonant frequency while $m = 1$ have the second lowest resonant frequency. Even though, $m = 0$ is the lowest resonant frequency, we consider $m = 1$ since the resonant frequency at $m = 0$ is zero while $m = 1$ gives the most uniform magnetic field in the center of the coil.

2.4 High-pass Birdcage Coil

The equivalent circuit model can be used to model high-pass birdcage coil. As shown in Figure 6, the coil is made up of equally spaced conductors (wires or strips) on a cylindrical surface, whose ends are connected to several capacitors. By modeling the conductors as inductors, the high-pass birdcage coil can be modeled as shown in Figure 13 [11].

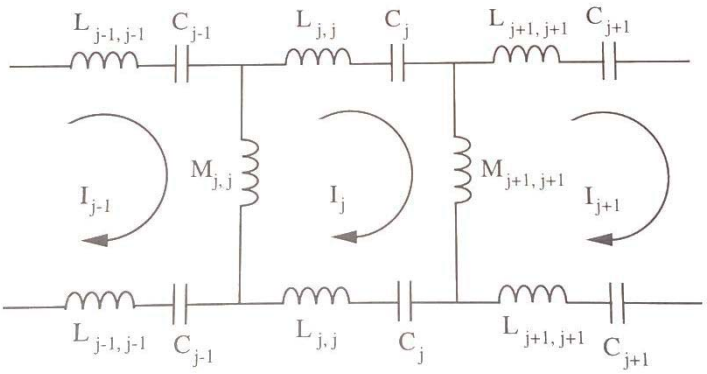

Figure 13: Current distribution of a high-pass birdcage coil

where M_{ij} denotes the self- inductance of the j^{th} element, M_{ij} denotes the capacitance of the capacitor connected between the j^{th} and $(j+1)^{th}$ legs, and L_{ij} denotes the self-inductance of the conductor used to connect to the capacitor. We neglect the mutual inductance by setting $C_1 = C_2 = \ldots = C$, $L_1 = L_2 = \cdots = L$ and $M_{11} = M_{22} = \ldots = M$. By applying Kirchhoff's voltage law,

$$i\omega M(I_j - I_{j-1}) - i\omega M(I_j - I_{j+1}) - 2i\omega L I_j + \frac{2i}{\omega C} I_j = 0 \ , \ j = 1, 2, \ldots, N \qquad (2.10)$$

Because of cylindrical symmetry, the current I_j must satisfy the periodic condition $I_{j+N} = I_j$. Eq. (2.10) will have the form given in Eq. (2.8). The resonant frequency is determined by substituting Eq. (2.8) into Eq. (2.10)

$$\omega_m = \left[C\left(L + 2M\sin^2\frac{\pi m}{N}\right)\right]^{-1/2},\ m = 0, 1, 2, \ldots, N \qquad (2.11)$$

For high-pass birdcage coils, the highest resonant mode occurs at $m = 0$. In this mode the current flows only in the end rings. If two modes have the same m, their resonant frequencies are the same and called degenerate modes. These two modes produce B_1 field which is perpendicular to each other as discussed in section 2.2. In order to generate a homogeneous B_1 field in the N-leg birdcage coil at the Larmor frequency, the current in the legs must be proportional to sin θ or cos θ, which corresponds to $m = 1$.

At higher frequencies, the RF coil size is comparable to the wavelength. Hence, the coil modeling using quasi-static technique does not work. Therefore, full-wave modeling of electromagnetic fields becomes necessary at higher frequencies. Over the years, many methods have been developed to model the fields in the birdcage. Some of the methods are finite element method (FEM) [10], finite-difference time-domain method (FDTD) [16], and method of moment [17]. In this thesis, we used the finite element method in COMSOL Multiphysics to model the birdcage coil. The capacitance value is swept to obtain homogenous B_1 field. The magnetic field homogeneity and specific absorption rate (SAR) are also investigated at various frequencies.

CHAPTER 3

BIRDCAGE COIL MODELING AT 64 MHz

As previously mentioned, the design of birdcage coil using lumped circuit element model begins to fail as the frequency increases and wavelength becomes comparable with the coil dimension. Therefore, more accurate modeling methods must be used in order to understand the interaction of the electromagnetic field with the object inside the coil. In this chapter, low-pass birdcage coil is used to obtain homogeneity using 3D finite element method (FEM) in COMSOL Multiphysics. The model is introduced with respect to geometry, physics, boundary conditions and mesh. Frequency domain analysis is used to obtain electromagnetic field solution of the birdcage coil at 64 MHz. The homogeneity is attained by quadrature excitation and optimal capacitance values of lumped elements in the coil. Parametric sweep is carried out to find the optimum capacitance value. Both air and head phantom domains are used to study the performance.

3.1 Finite Element Modeling of a Birdcage Coil

In this section, we built FEM model of low-pass birdcage coil in order to calculate optimum capacitance values to obtain homogenous magnetic field inside the birdcage coil. As seen from Figure 14, the geometry of the model consists of circular loops (rings) having radius of 0.24 m, eight equally spaced rungs (legs) with each length of 0.3 m and three capacitors with each length of 0.01 m placed in each rung [18].

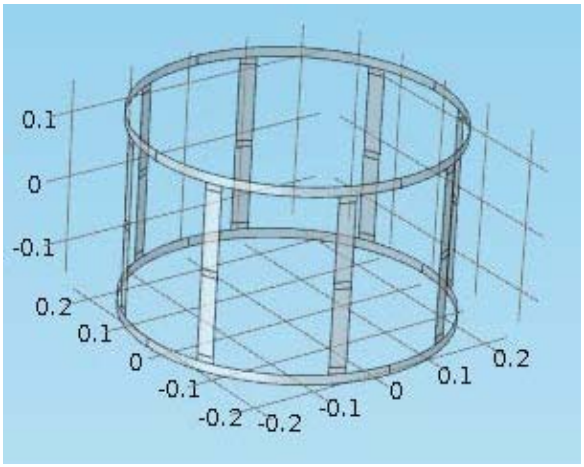

Figure 14: Geometric model of a low-pass birdcage coil

Before using parametric sweep to find the value of the capacitance of the lumped elements, we used the capacitance value set by using ϵ_r the relative permittivity of the material assigned to the capacitor using the formula

$$C = \epsilon_0 \epsilon_r \frac{A}{d} \tag{3.1}$$

where ϵ_0 is the permittivity of free space, A is the area of parallel plates and d is the distance between the parallel plates.

After building the geometry of the coil, the next step is setting up the physics for the model using Electromagnetic Waves interface added under the Radio Frequency branch for the physics section of the model.

The interface that solves the electromagnetic wave equation of time harmonic is given as

$$\nabla \times \mu_r^{-1} (\nabla \times \mathbf{E}) - k_0^2 \left(\epsilon_r - \frac{j\sigma}{\omega \epsilon_r}\right) \mathbf{E} = 0 \tag{3.2}$$

$$k_0^2 = \omega \sqrt{\epsilon_r \mu_0} \tag{3.3}$$

where $\mathbf{E}$ is the electric field, μ_r is the relative permeability, σ is the conductivity and k_o is the wave number of free space.

After adding physics, boundary conditions are assigned to the surface of the coil elements and the outer boundary of the solution domain enclosing the coil geometry. The coil surface and the shield around the coil are assigned the perfect electric conductor (PEC) condition. PEC boundaries of the birdcage coil are shown in Figure 15.

One of the challenges when modeling using finite element method is how to prevent reflection from the outer boundary enclosing the coil geometry. Scattering boundary condition is then used to avoid any reflection of the outgoing wave from the exterior boundary of the computational domain as shown in Figure 16.

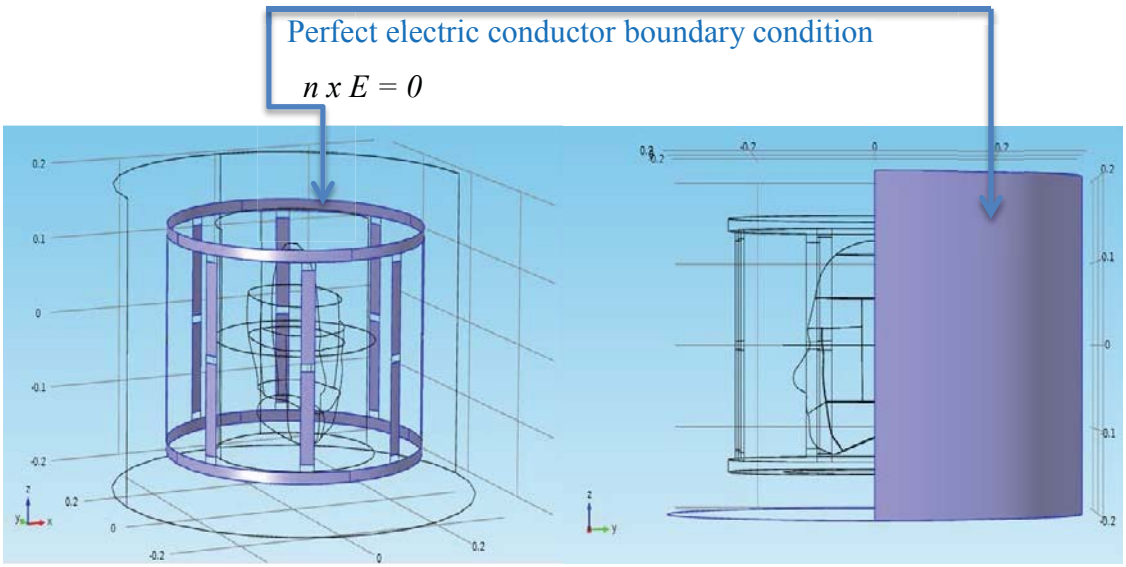

(a) (b)

Figure 15: (a) PEC boundaries: rungs, end rings (b) cylindrical conductive shield. The front of the shield is removed for visualization

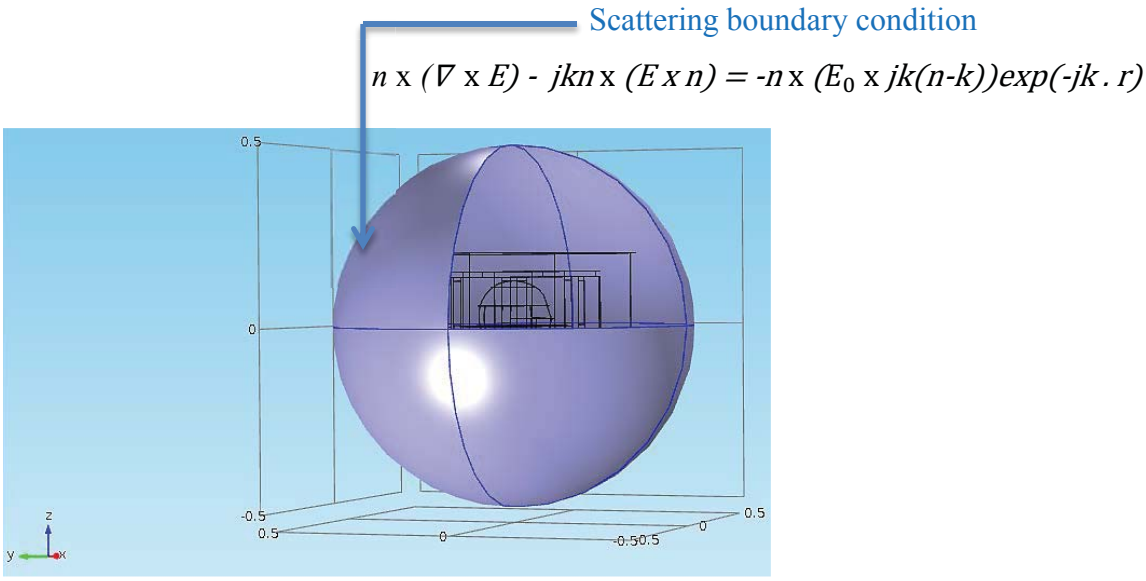

Figure 16: Sphere boundary assigned to a scattering boundary condition

At last, lumped ports are used to provide quadrature excitation. Equation for lumped port is given as

$$Z_{port} = \frac{V_{port}}{I_{port}} \tag{3.4}$$

Here, V_{port} is the voltage along the edges (5000 Volts), I_{port} is the electrical current magnitude, and Z_{port} is the input impedance. The lumped port is where the voltage or current is applied must be placed between metallic type boundaries as in this case in a PEC.

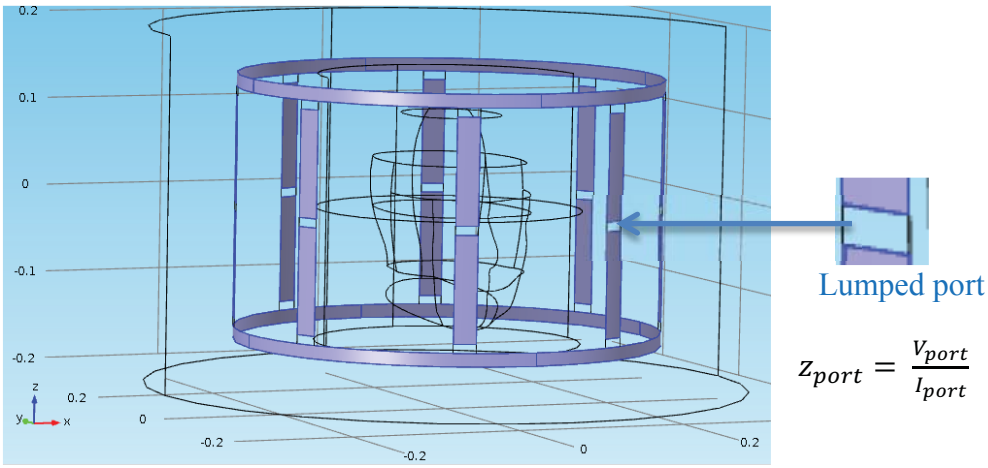

Figure 17: Two-port excitation using lumped port

After adding physics and boundary conditions, fine mesh is specified to obtain good approximation of the birdcage coil. The 3D model is discretized using triangular and tetrahedral elements as shown in Figure 18. The numbers of tetrahedral and triangular elements are found to be 68,785 and 5,282 without the human head phantom. However, the number is increased when using the human head phantom to 79,785 tetrahedral and 6,166 triangular elements. The maximum element size is 0.08 m.

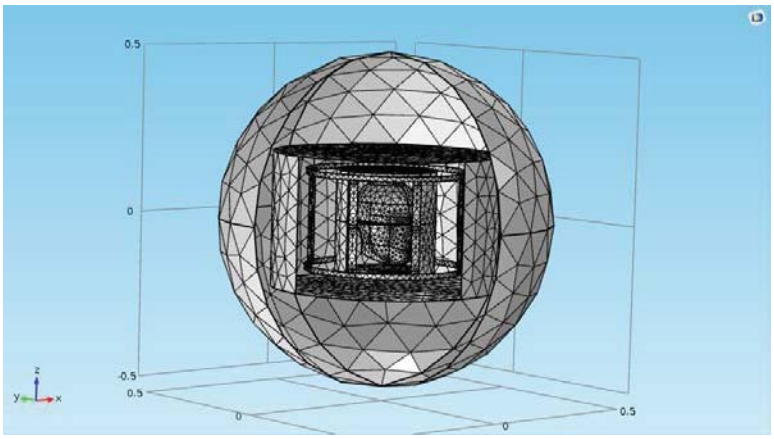

Figure 18: Mesh structure of low-pass birdcage coil

3.2 Frequency Domain Analysis of a Birdcage Coil

After modeling the low-pass birdcage coil using FEM, we performed frequency domain analysis. This analysis is used to solve the electromagnetic fields of a birdcage coil for a given frequency. In addition, COMSOL Multiphysics allows us to specify more than one frequency in order to observe the variation of any electromagnetic field parameter with respect to the frequency. For instance, we can inspect the return loss (S_{11}) by running simulations for a range of frequencies (frequency sweep) to see where we have smaller return loss within specified capacitance value. Using this analysis, we are able to observe the B_1 field distribution inside the coil, SAR values inside the coil and surface current distribution along the legs and end rings.

3.3 Quadrature Excitation

In the frequency domain analysis, quadrature excitation is used to obtain homogeneous and circularly-polarized magnetic field in the birdcage coil by properly tuning the capacitors. Quadrature excitation is driven from two ports which are equal in magnitude but with a phase of 90^0 to generate circularly-polarized field inside the coil. As mentioned in section 2.2 for mode m = 1, quadrature excitation generates circularly-polarized field which is more homogeneous than linear excitation as a result of equal currents distribution along the legs of the coil.

In addition, quadrature driven birdcage coil is more power efficient compared with linear drive, by reducing the RF power requirement by a factor of two. Linear B_1 field can be broken up into two circularly-polarized fields $\mathbf{B_1}^+$ and $\mathbf{B_1}^-$.

$$\mathbf{B}_{linear} = B_1 \cos(\omega t)\hat{x} = \left(\mathbf{B_1}^+\right) + \left(\mathbf{B_1}^-\right) \tag{3.5}$$

where $\mathbf{B_1}^{\pm} = \frac{B_1}{2}\left(\cos(\omega t)\hat{x} \pm \sin(\omega t)\hat{y}\right)$.

The first term represents a right-circularly polarized field while the second term represents left-circularly polarized field having equal magnitude of $B_1/2$. The power consumption of a coil is proportional to the coil current while the magnetic field it produces is proportional to current. As a result, the power consumption is directly proportional to the square to the magnetic field it produces

$$\mathrm{P}_{linear} = \propto \left(\mathbf{B_1}^+\right)^2 + \left(\mathbf{B_1}^-\right)^2 \propto 2\left(\mathbf{B_1}^+\right)^2 \tag{3.6}$$

If we apply

$$\mathbf{B_1}^+ = \frac{B_1}{2}\left(\cos(\omega t)\hat{x} + \sin(\omega t)\hat{y}\right) \tag{3.7}$$

Then,

$$\mathrm{P}_{quadrature} = \propto \left(\mathbf{B_1}^+\right)^2 = \frac{1}{2}\mathrm{P}_{linear} \tag{3.8}$$

3.4 Capacitance Tuning Using Parametric Sweep

The designed birdcage coil has basic RLC components and it needs to resonate at the Larmor frequency. Initial tuning began by calculating the capacitance value, which is necessary for the coil to resonate at the desired frequency (64 MHz). The capacitor is then tuned in order to obtain homogeneous magnetic field for an air phantom, a parametric sweep is carried out for the capacitance of the coil's lumped element using COMSOL Multiphysics. The air phantom has a material property of electrical conductivity σ = 0 S/m, relative permeability μ_r = 1 and relative permittivity $\epsilon_r = 1$. The capacitance values range from 20 pF to 30 pF with a step capacitance of 0.5 pF for a given frequency value (64 MHz). The simulation is conducted on a 4-core workstation with Intel(R) Xeon(R) CPU @3.50 GHz and 16 GB RAM. Tuning the capacitance without the head phantom took memory size of 2.7 GB with a run time of 515 sec.

Figure 19 shows the integration of the magnetic flux density in order to find the circularity of the field [18]. The circularity is evaluated by estimating the sum of the axial ratio of the magnetic field given as $20\log_{10}((\mathbf{B}_{right}+\mathbf{B}_{left})/(\mathbf{B}_{right}-\mathbf{B}_{left}))$. Where $\mathbf{B}_{left}$ denotes the left hand rotating component of magnetic flux while $\mathbf{B}_{right}$ denotes the right hand rotating component of magnetic flux. Respectively the homogeneity of the field is calculated using the standard deviation of the electric field [18]. As seen from Figure 20, the optimal capacitance value for field homogeneity is the same as that for circularity. From the plot, it can be seen the optimal value of the capacitance is close to 27.5 pF.

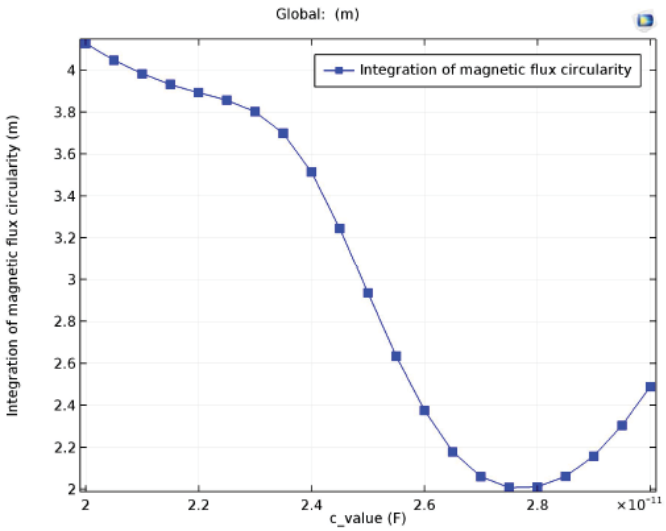

Figure 19: The axial ratio of the magnetic flux density for coil only at 64 MHz

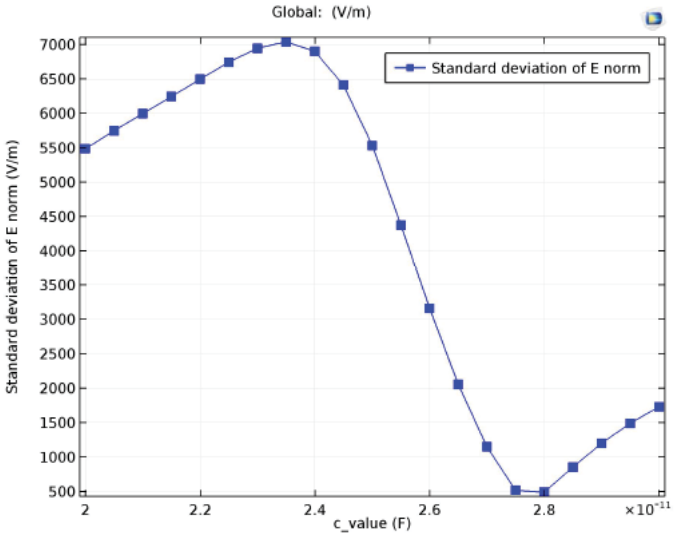

Figure 20: The standard deviation of the electric norm for coil only at 64 MHz

3.5 Magnetic Field Homogeneity

The simulation has been made for 8-leg low-pass birdcage coil loaded with air phantom. Capacitance value used on the rungs is 27.5 pF and the simulation frequency is 64 MHz. Total number of degrees of freedom solved for this model is 437,214. The memory used for this simulation is 2.34 GB. The physical memory size used for this simulation is 2.34 GB with a total run time of 30 second.

A homogenous magnetic field around the air phantom at 64 MHz is shown in Figure 21. In addition, the real part of the magnetic flux is almost orthogonal to the imaginary part of it, which indicates the flux is rotating circularly.

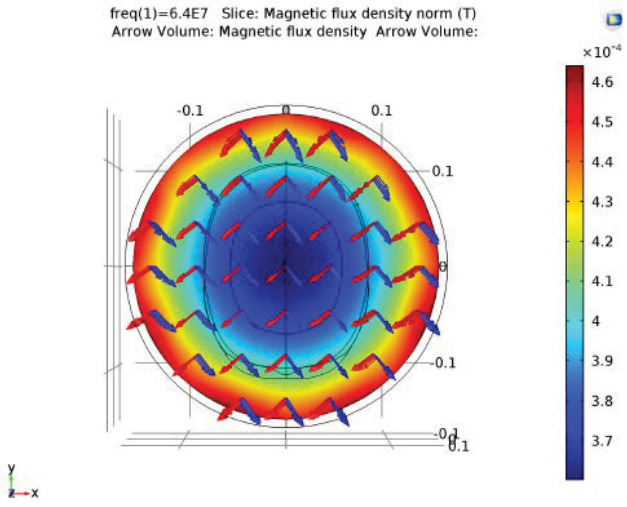

Figure 21: Magnetic flux density norm distribution with the real (red) and imaginary (blue) part of the magnetic flux density for coil only at 64 MHz

For the air phantom, we are able to get excellent magnetic field homogeneity and circularity. However, the problem arises when the human head is placed with in the RF coil. As a result, the head phantom significantly changes the magnetic field homogeneity and circularity. This is due to two major reasons. First, the wavelength in the head is smaller than the empty coil. Second, the head induces additional non-uniform currents on the coil elements due to the dielectric properties of tissues. The head is modeled using skin material properties, relative permittivity ϵ_r = 73, relative permeability $\mu_r = 1$ and electrical conductivity σ = 0.73 S/m. As seen from Figure 22, the circularity and homogeneity of the field are distorted due to the high dielectric loading (human head phantom). The total number of degrees of freedom solved for this

model is 505,464. The physical memory size used for this simulation is 2.55 GB with total run time of 36 sec.

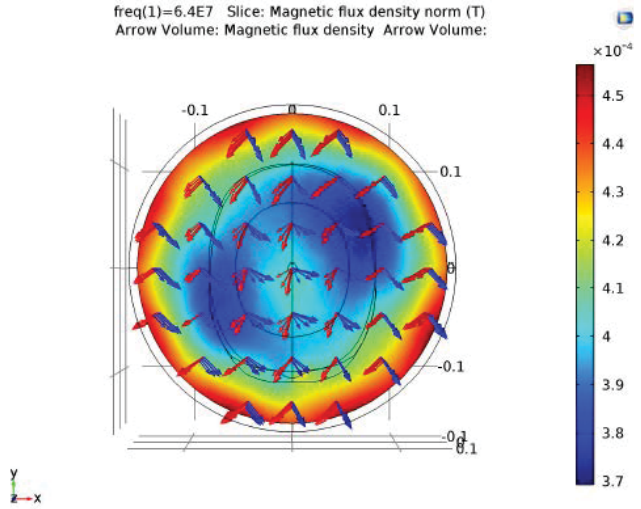

Figure 22: Magnetic flux density norm distribution with the real (red) and imaginary (blue) part of the magnetic flux density loaded with human head phantom of skin tissue property at 64 MHz

Optimum capacitance value can be found by tuning the capacitor further. One can also observe the electric field generated by an empty coil with quadrature excitation shown in Figure 23. From the plot, we observe the electric field varies linearly in the radial direction with a minimum at the center. This results in a uniform magnetic field with a circular polarization.

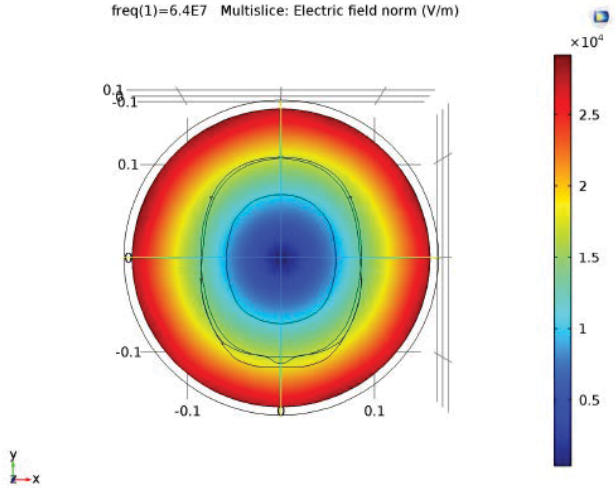

Figure 23: Electric field norm (V/m) of unloaded birdcage coil at 64 MHz

Next, we use brain tissue property of relative permittivity ϵ_r = 88 and electrical conductivity σ = 0.49 S/m. As shown in Figure 24, B_1 field inside the birdcage coil is highly distorted and experience a high magnetic field in the center region. Comparing the results for two different tissue properties, we can see that increasing in the relative permittivity leads to a higher B_1 field in the center region. The total number of degrees of freedom solved for this model is 494,456. The physical memory size used for this simulation is 2.55 GB with a run time of 34 sec.

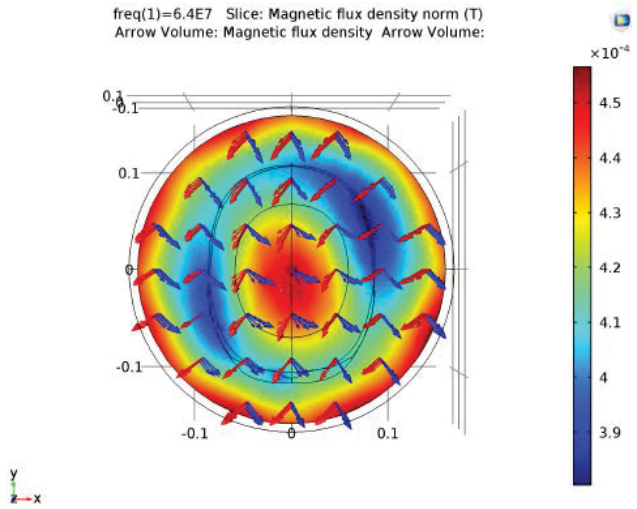

Figure 24: Magnetic flux density norm distribution with the real (red) arrow and imaginary (blue) part of the magnetic flux density loaded with human head phantom of brain tissue property at 64 MHz

Next we plot the current distribution in the coil without the head as shown in Figure 25. In order to get homogenous magnetic field inside the coil, the currents in the rungs of the coil are required to have a sinusoidal distribution. The following analysis is based on equivalent circuit model for quadratic excitation, the current in the eight elements are distributed according to [10].

$$I_i = \frac{I_0}{2} \cos\left(\frac{(i-1)\pi}{4} + j \sin\frac{(i-1)\pi}{4}\right) \tag{3.9}$$

where I_i is the current in the i^{th} element. Eq. (3.9) is only valid when the coil is small compared to the wavelength. Therefore, as the size of the coil increase, there will be a significant interaction between the coil and the human head.

As mentioned in the previous chapter, for low-pass birdcage coil, homogenous B_1 field occurs at m = 1. Therefore, we used the first resonant mode (m = 1) to produce sinusoidal current distribution in the rung elements and generate uniform B_1 field in the transverse plane as shown in Figure 25 (a).

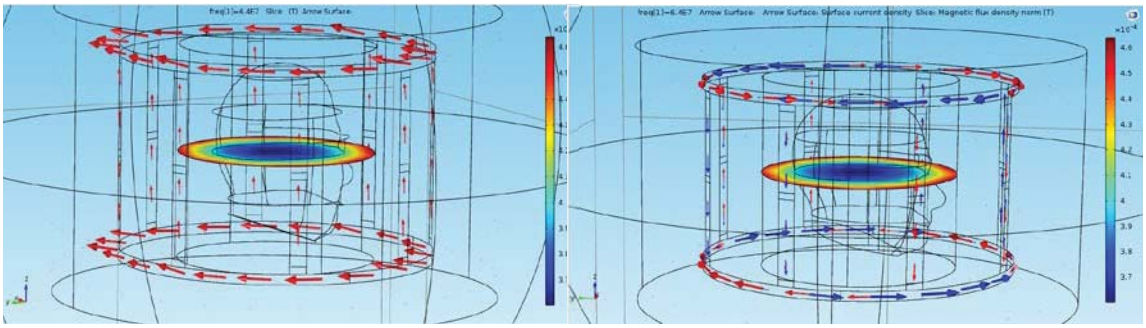

(a) (b)

Figure 25: (a) Magnitude images of B_1 field and the arrow plot of magnitude of current density at 64 MHz (b) Surface current density with an arrow of the real part (blue) and the imaginary part (red) at 64 MHz

The current distribution as shown in Figure 25 (b) is divided into real (blue) and imaginary (red); by using Eq. (3.9) we are able to calculate the current in each rung. For 8-leg birdcage coil, there is no current flow in the 3rd and 7th rung element since the cosine value (real part) is zero. On the contrary, there is no current flow in the 1st and 5th rungs element since the sine value is zero (imaginary part). By taking the absolute value of the Eq. (3.9), we have an equal magnitude of current flow as seen from Figure 25 (a).

3.6 Overview of Dielectric Properties of Human Tissues

Understanding the dielectric properties of human tissues is important to study the electromagnetic interaction with the human head. As mentioned in section 3.5, such interaction degrades the B_1 field due to the dielectric resonance of exposing tissues to high temperature caused by increased SAR.

Each tissue reacts differently when exposed to RF. Therefore, it is imperative to know the dielectric properties of tissue for a given frequency. Throughout the years researchers provided theories formulated to explain the dielectric properties. More extensive literature reviews of dielectric properties have been provided by Stuchly and Stuchly [20] and Simunic [21]. Recent development in the field of electromagnetic

dosimetry evaluates the internal fields within the exposed structure to produce high-resolution from medical imaging data [21]. Dielectric properties of the human anatomy in the frequency range 10 KHz to 10 GHz over 30 tissue types are discussed [22]. However, there is no consensus on the dielectric data. In this thesis, we will only use both the skin and brain tissue parameters as the human head properties.

Table 1: Human tissue parameters

Tissue type ρ (g cm^{-3})		64 MHz		128 MHz		171 MHz	
		ϵ_r	σ (S/m)	ϵ_r	σ (S/m)	ϵ_r	σ (S/m)
CSF	1.06	106	0.62	103	0.7	74	2.21
Air		1	0	1	0	1	0
Muscle	1.04	85	0.89	65	1.3	60	0.78
Bone	1.85	26	0.04	25	0.05	14	0.08
Skin	1.10	73	0.73	63	0.86	53	0.61
Lens	1.05	46	0.45	35	0.45	39	0.34
Humor	1.01	100	1.9	73	1.7	69	1.51
Brain	1.03	88	0.49	70	0.57	53	0.53
Cartilage	1.10	26	0.04	25	0.05	48	0.54

The dielectric properties of materials are obtained from the complex relative permittivity of the materials are expressed as

$$\hat{\epsilon} = \epsilon_r - j\epsilon'' = \epsilon_r - j\frac{\sigma}{\epsilon_0 \omega} \tag{3.10}$$

where ϵ'' is the out-of-phase loss factor, σ is the electric conductivity, ϵ_0 is the permittivity of free space and ω is the angular frequency of the field. From Eq. (3.10), we observe that the dielectric properties are highly dependent on the frequency.

3.7 Specific Absorption Rate (SAR) at 64 MHz

When the human head is placed inside the birdcage coil, there is an interaction between the electromagnetic fields and biological tissues. The most common parameter used to assess the exposure of RF electromagnetic fields generated by the coil is given in terms of the specific absorption rate (SAR). SAR is the rate at which the RF energy is absorbed at a given time by a specific mass of tissue. The amount of electromagnetic radiation within each tissue layer is dependent on the tissue properties. Figure 22 shows the homogeneity deteriorates when the head phantom is placed in the birdcage coil.

Thus the inhomogeneity leads to local exposure where most of the absorbed energy is applied to one body region, which causes a health concern as the temperature rises due to RF deposition. As the magnetic field exceeds 1.5 Tesla, violation of local specific absorption rate (SAR) for FDA limit (8 watts/kg) in any gram over the head with a five-minute exposure, can be a major health concern issue [19]. In this section, we calculate the SAR to understand the RF heating in the human head phantom.

The equation of SAR is given as

$$\text{SAR} = \frac{\sigma|\mathbf{E}^2|}{2\rho} \tag{3.11}$$

where σ (S/m), ρ (kg/m^3) and $|\mathbf{E}|$(V/m) are the conductivity, mass density of the tissue and magnitude of the electric field in the tissue. SAR can be tested for different tissues in The head including skin, muscle, bone, brain, cerebrospinal fluid (CSF), air (sinuses), lens humor and cartilage. Their material properties are given in Table 1. The permittivity and conductivity of the tissues are obtained by interpolation and extrapolation of the data given by Stuchly and Stuchly [20] and Simunic [21].

Using COMSOL Multiphysics, the SAR results are tested for 64 MHz using brain tissue as given in Table 1, that is ϵ_r = 88 and σ = 0.49 S/m. The same lumped port is applied by using 1 Volt to excite the two lumped ports. Figure 26 displays the axial, sagittal and coronal slices of the SAR distribution calculated inside the human phantom model at 64 MHz. As seen from Figure 26, the SAR increases in the area near the coil and starts to decrease as it gets close to the center as a result a of weak electric field. The average and maximum SAR is calculated in Table 2. The human head phantom is given as a brain tissue property; however, unless the SAR values are tested for a specific organ we will not get accurate SAR results. The highest SAR occurs between the nose and eye area of the skin region. The dielectric properties of tissues determine the SAR distribution. The penetration of the electromagnetic waves into the head decreases rapidly along the distance. This can be measured using skin depth as shown in Eq. (3.12),

$$\delta = \sqrt{\frac{2}{\omega\mu\sigma}} \tag{3.12}$$

If the skin depth is smaller than the wavelength, scattering boundary conditions must be used. In addition, when the skin depth is comparable to or larger than the size of the object, the electromagnetic waves will penetrate into the object causing high SAR in the tissues.

Table 2: Maximum and average SAR at 64 MHz

Tissue type	64 MHz	
	Ave (kg/m^3)	Max (kg/m^3)
Brain	0.000911	0.00846

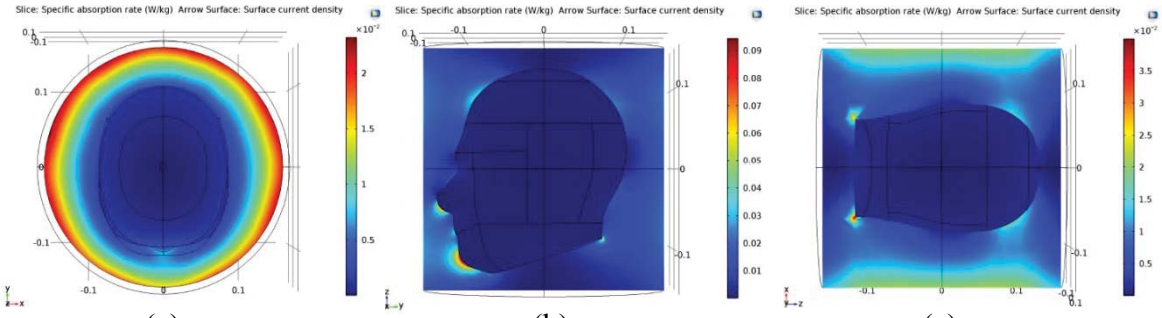

(a) (b) (c)

Figure 26: Sliced SAR distribution (a) axial (b) sagittal and (c) coronal slices of the human phantom at 64 MHz

3.8 Convergence Study

The Finite element method (FEM) is a well-known numerical method in solving partial differential equations (PDE). All numerical methods have an error in comparison to the true solution of the PDE. One known method to study the sensibility of the numerical solution is the convergence study [23]. The convergence study compares two consecutive meshes by refining the mesh to a specific size to get close to the true solution with pre-specified error tolerance.

Using both loaded and unloaded cases for different meshes, we are able to determine if our simulation result converges. The maximum element size is set to be $\lambda/6$. The maximum mesh element size has to be less than λ/6 to converge as shown in Table 3. The uniformity of B_1 field and orthogonality of the magnetic flux does not change as we change the mesh type from fine to extremely fine as seen in Figure 27 and

28. From our simulation, we conclude all the results for the 64 MHz birdcage coil as the number of meshes increases.

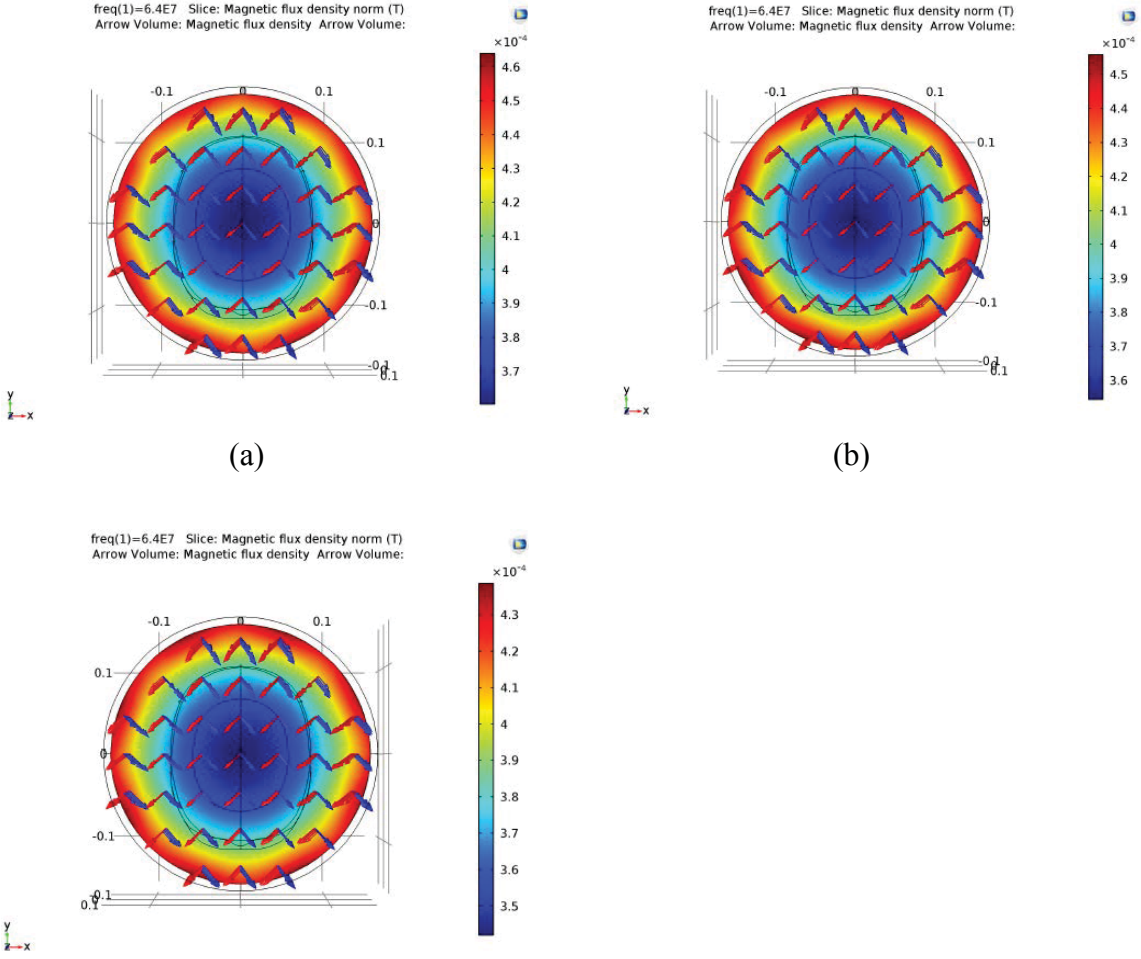

(a) (b)

(c)

Figure 27: Magnetic flux density norm distribution with an arrow of the real (red) and imaginary (blue) part of the magnetic flux density for coil only using (a) fine mesh (b) finer mesh and (c) extra fine mesh at 64 MHz

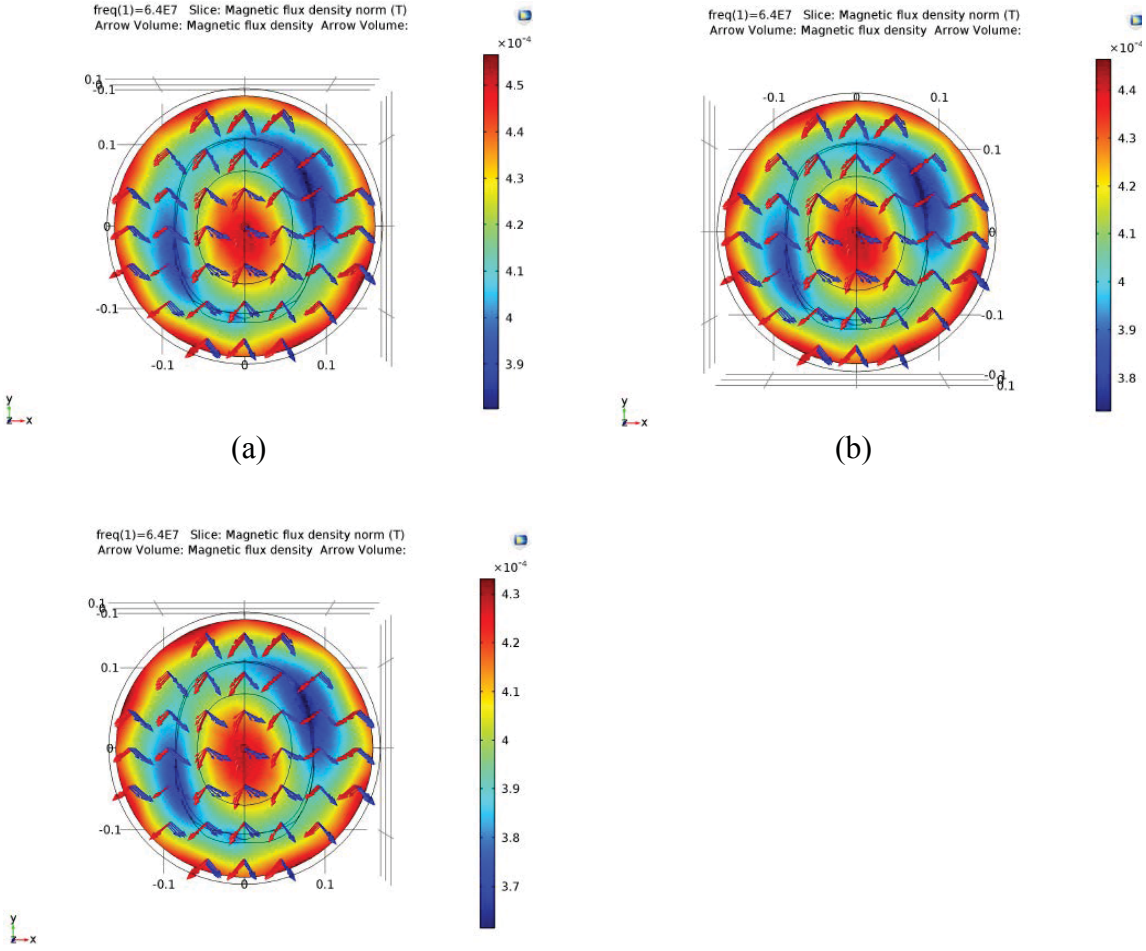

Figure 28: Magnetic flux density norm distribution with an arrow of the real (red) and imaginary (blue) part of the magnetic flux density when loaded with human head phantom using (a) fine mesh (b) finer mesh and (c) extra fine mesh at 64 MHz

Table 3: Number of elements and maximum element size for different types of meshes at 64 MHz

Frequency	Mesh type	Tetrahedral element (unloaded)	Tetrahedral element (loaded)	Maximum element size (m)
64 MHz	Fine	68,785	79,359	0.08
	Finer	106,854	110,676	0.055
	Extra fine	181,011	181,011	0.035

CHAPTER 4

BIRDCAGE COIL MODELING AT 127.5 MHz and 170 MHz

In this chapter, we will analyze the birdcage coil at higher frequencies (127.5 MHz and 170 MHz). Increasing the frequency will distort the good homogeneity and circularity of the magnetic field. However, by tuning the capacitor, we can achieve good homogeneity and circularity.

4.1 Capacitance Tuning Using Parametric Sweep

Using parametric sweep, we are able to tune the capacitance of the lumped elements to obtain homogenous and circular B_1 field at the Larmor frequency for the air phantom. The capacitance values range from 0 pF to 7 pF with a step capacitance of 0.2 pF for a given frequency value of 127.5 MHz. Tuning the capacitance without the head phantom takes a memory size of 2.66 GB with a run time of 815 sec. The circularity and homogeneity of the magnetic field are evaluated using standard deviation of the electric field and integration of the axial ratio of the magnetic flux. From Figure 29 and 30, we observed the optimal value for the capacitance is close to 4.8 pF.

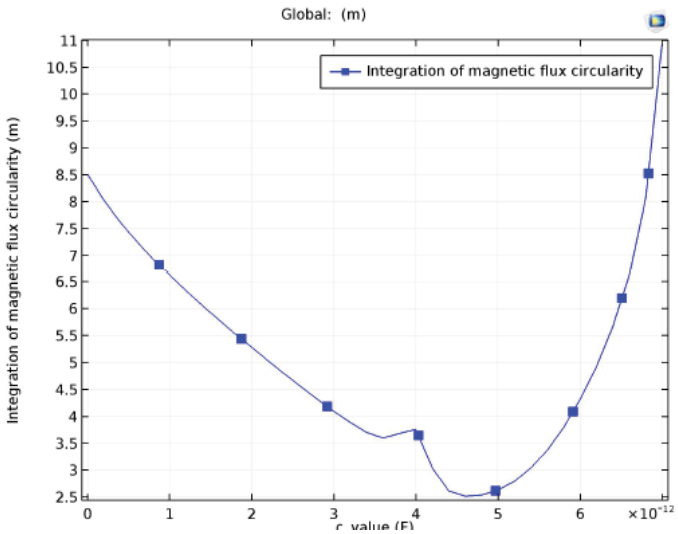

Figure 29: The axial ratio of the magnetic flux for coil only at 127.5 MHz

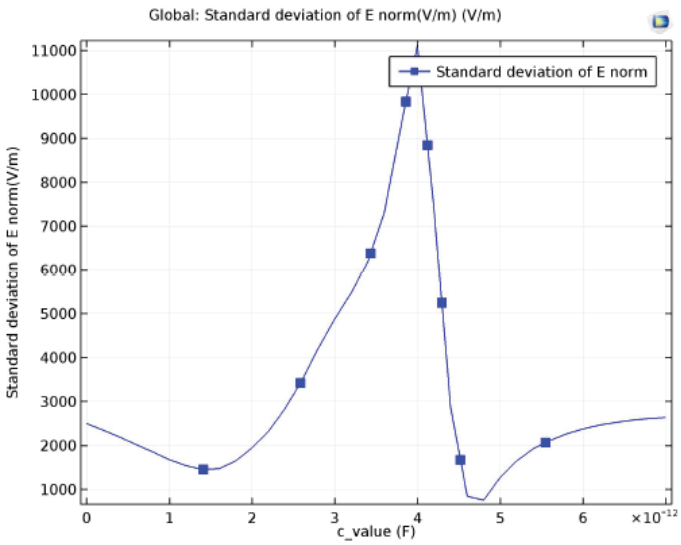

Figure 30: The standard deviation of the electric norm for coil only at 127.5 MHz

The same procedure is used to calculate homogeneity and circularity of the magnetic field for 170 MHz. The capacitance values for the simulation range from 0 pF to 3.5 pF with a step capacitance of 0.2 pF for a given frequency value of 170 MHz. Tuning the capacitance without the head phantom takes memory size of 2.8 GB with a run time of 614 sec.

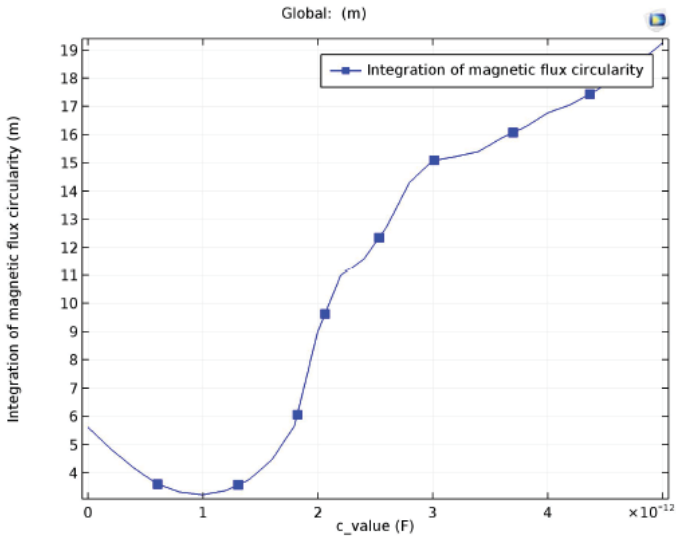

Figure 31: The axial ratio of the magnetic flux density for coil only at 170 MHz

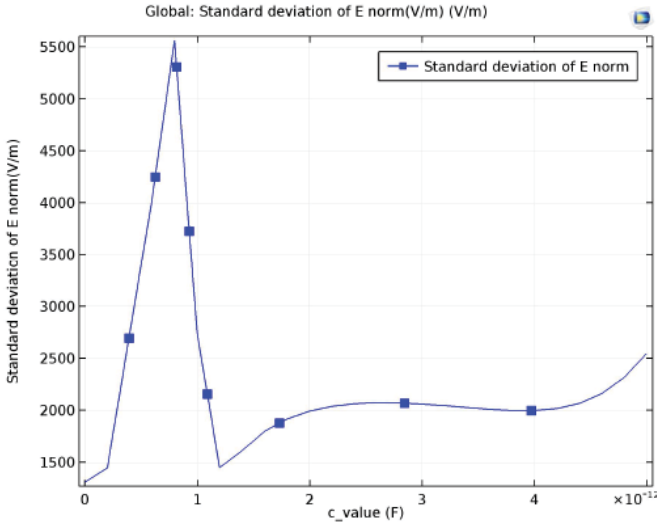

Figure 32: The standard deviation of the electric norm around for coil only at 170 MHz

The parametric sweep indicates the optimal value to satisfy these two requirements (circularity and homogeneity) is around 1 pF and 1.2 pF at 170 MHz as shown in Figures 31 and 32. However, 1 pF gives the more uniform magnetic field inside the coil compared to 1.2 pF therefore, we use 1 pF as the optimal capacitance value.

4.2 Magnetic Field Homogeneity

The simulation performed for the 8-leg low-pass birdcage coil around the air phantom at 127.5 MHz is shown in Figure 33. The number of degrese of freedom in the equation system is about 437,214 while using 2.51 GB physical memory with a total run time of 29 sec. The number of tetrahedral elements is found to be 68,785 with a maximum element size of 0.08 m. As seen from Table 4, the magnetic field near and inside the coil is lower compared to 64 MHz. However, the birdcage coil at 127.5 MHz still maintains homogenous and circular magnetic field around the air phantom. Figure 34 shows the coil loaded with the human head phantom. The human head phantom is modeled using the brain tissue parameters of , σ = 0.57 S/m, $\mu_r = 1$ and ϵ_r = 70. Total number of degrees of freedom in the equation system is about 510,044. The memory size used for this simulation is 2.63 GB with total run time of 0.08 sec. As seen from the

figure the circularity and homogeneity of the field is distorted due to the dielectric material property of the human head phantom impeding sinusoidal current flow.

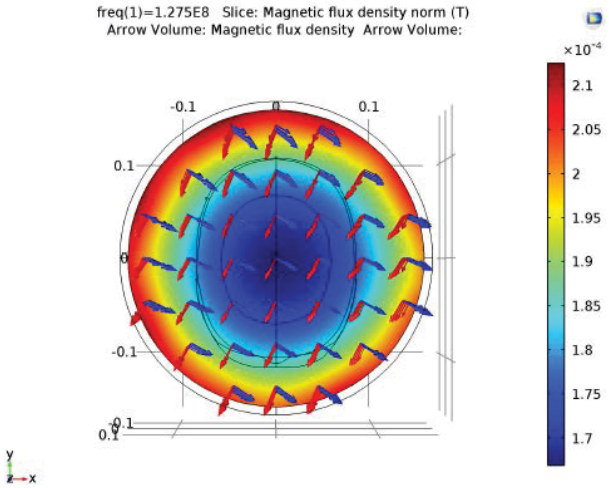

Figure 33: Magnetic flux density norm distribution with the real (red) and imaginary (blue) part of the magnetic flux density for coil only at 127.5 MHz

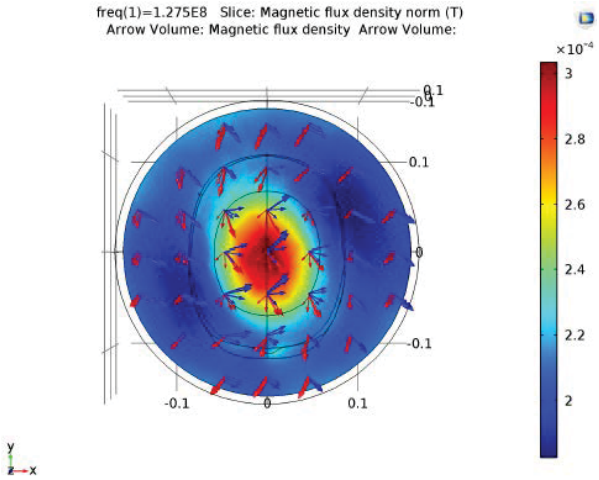

Figure 34: Magnetic density norm distribution with the real (red) and imaginary (blue) part of the magnetic flux density loaded with human head phantom using brain tissue at 127.5 MHz

Table 4: Magnetic field distribution near and inside the coil for air domain

Near to the coil B_1 field (T)	Inside the coil B_1 field (T)	Frequency (MHz)
4.2 to 4.5x10^{-4}	3.5 to 4x10^{-4}	64
1.95 to 2.1x10^{-4}	1.7 to 1.9x10^{-4}	127.5
2.25 to 2.35x10^{-4}	1.91 to 2.1x10^{-4}	170

Since the optimal capacitance value to achieve homogeneity and circularity is not equal at 170 MHz, the field distribution around the air and human head phantom is computed. Comparing the results, we get better homogeneity and circularity result while using 1 pF. Using the same material properties (air), the magnetic field distribution is shown in Figure 35. The degrees of freedom in the equation system is 439,992, while taking 2.55 GB memory size with a total run time of 31 sec. The number of tetrahedral elements is found to be 69,219 with a maximum element size of 0.2939 m.

The human head is placed to see the interaction with B_1 field. The brain of the human head phantom at 170 MHz is modeled using the material properties of σ = 0.53 S/m, $\mu_r = 1$ and ϵ_r = 53. As seen from Figure 35, B_1 field is substantially degraded as well as the quality of the image. It is also a concern to safety because the electric field associated with the increase of inhomogeneity of the B_1 field. Some part of the body, such as the brain and eyes can be sensitive to high SAR. Total number of degrees of freedom in the equation system is about 514,018 while the memory size used is 2.66 GB with total run time of 37 sec.

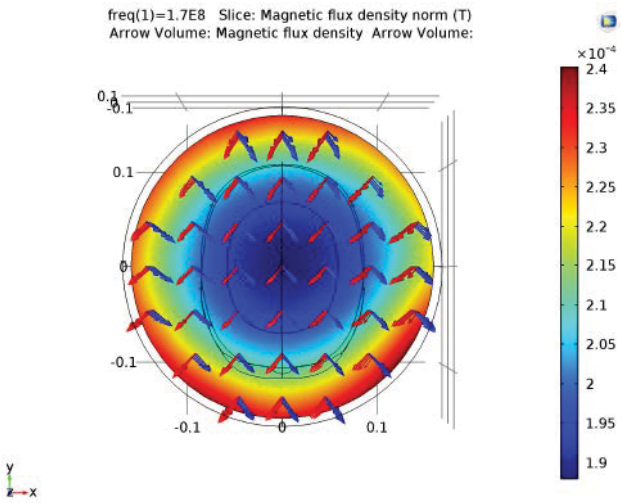

Figure 35: Magnetic flux density norm distribution with the real (red) and imaginary (blue) part of the magnetic flux density for coil only at 170 MHz

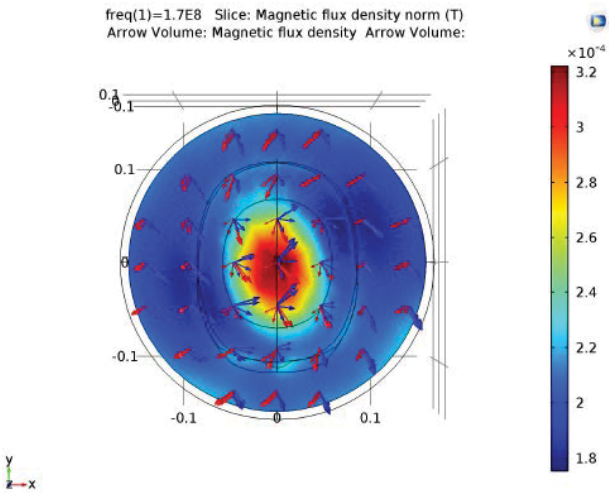

Figure 36: Magnetic density norm distribution with the real (red) and imaginary (blue) part of the magnetic flux density loaded with human head phantom at 170 MHz

4.3 Specific Absorption Rate (SAR) at 127.5 MHz and 170 MHz

As shown in Figures 37 and 38, the SAR is displayed in three planes at two different frequencies. The highest SAR occurs close to the coil carrying the maximum current while the smallest SAR at the center of the coil. From the sagittal and coronal slice, the top and bottom part of the head has relatively lower SAR. The human head phantom is modeled using brain tissue parameters summarized in Table 5. The average and maximum SAR of the head is given in Table 6. Compared to 64 MHz, both average and maximum SAR for 127.5 MHz and 170 MHz increase. Accurate SAR values can be determined if tested for a specific region of the head since the change in SAR with frequency would be different.

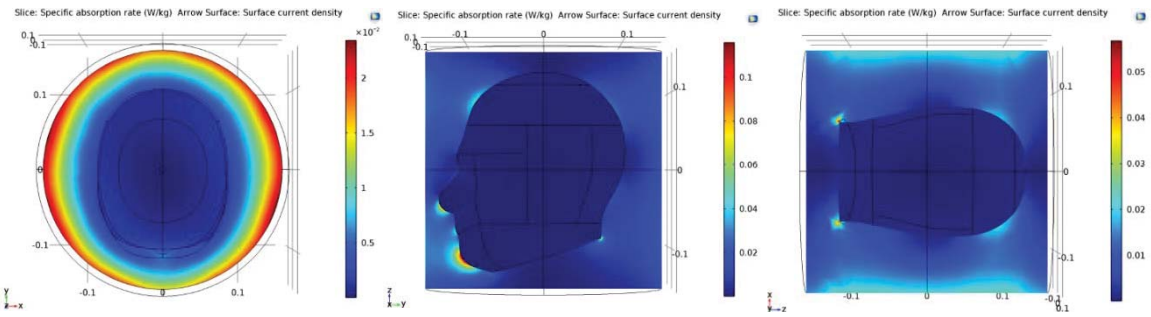

(a) (b) (c)

Figure 37: Sliced SAR distribution (a) axial (b) sagittal and (c) coronal slices of the human phantom at 127.5 MHz

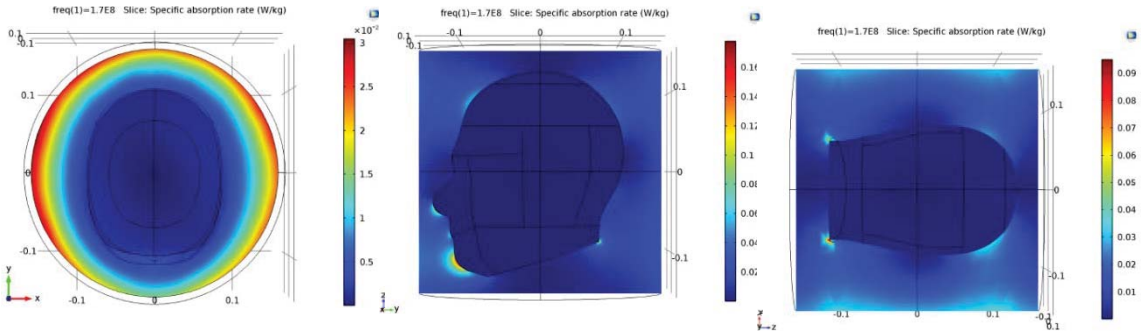

(a) (b) (c)

Figure 38: Sliced SAR distribution (a) axial (b) sagittal and (c) coronal slices of the human phantom at 170 MHz

Table 5: Brain tissue parameters

Tissue type	ρ(kg m^{-3})	127.5MHz		170 MHz	
		ϵ_r	σ (S/m)	ϵ_r	σ (S/m)
Brain	1030	70	0.57	53	0.53

Table 6: Maximum and average SAR at 127.5 and 170 MHz

Tissue type	127.5 MHz		170 MHz	
	Ave (kg/m^3)	Max (kg/m^3)	Ave (kg/m^3)	Max (kg/m^3)
Brain	0.00063	0.00457	0.0011	0.00577

The electric fields inside the coil are shown in Figure 39. Compared to 64 MHz, 127.5 MHz and 170 MHz have higher electric field leading to high SARs for higher frequencies.

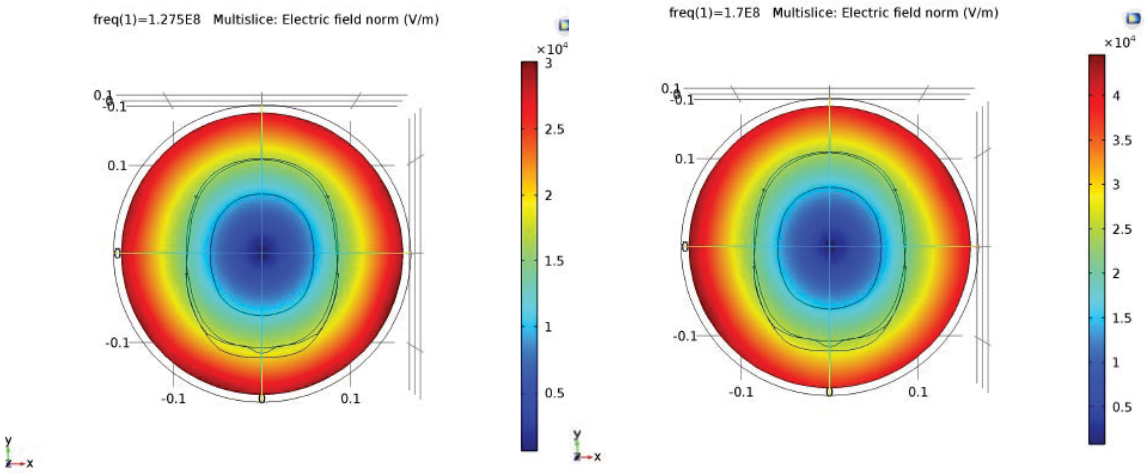

Figure 39: Electric field norm of unloaded quadrature coil at 127.5 MHz and 170 MHz

As discussed in Chapter 3, in order to get homogenous magnetic field inside the coil (transverse plane), the current on the rungs elements are required to have a sinusoidal distribution. Figure 40 shows the arrow plot of the surface current density in rungs for 127.5 MHz and 170 MHz.

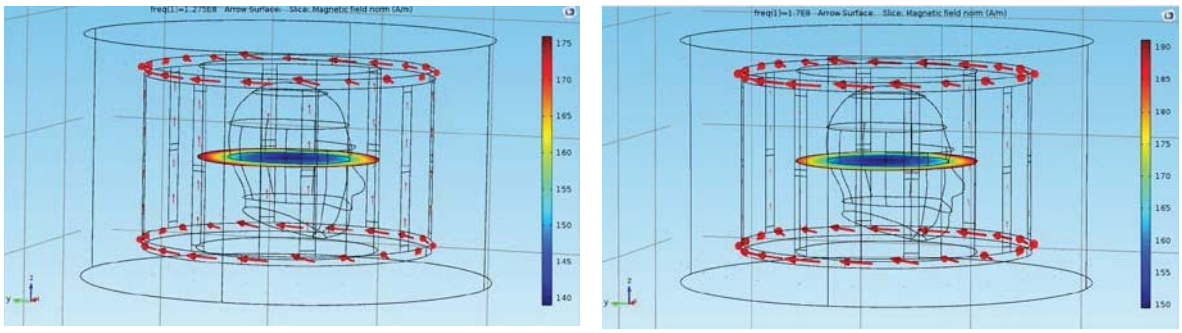

(a) (b)

Figure 40: Magnitude images of magnetic field and arrow plot of surface current densities for frequencies at (a) 127.5 MHz and (b) 170 MHz

4.4 Four-Port Excitation

Using the same geometry model, 4-port excitation is implemented to exhibit a good transverse magnetic field and specific absorption rate (SAR). As we increase the frequency (>170 MHz), the homogeneity deteriorates. In order to recover the homogeneity, the field distribution within the resonator must be modified. This can be accomplished by increasing the number of excitation port feeding the coil. By perfectly exciting each port with the same current amplitude in a manner similar to antenna array concept, a uniform magnetic field can be generated.

The idea behind the four-port excitation is similar to that of quadrature excitation. It involves feeding four equal amplitude RF signals with fixed phases 0^0, 90^0, 180^0 and 270^0 across four capacitors on the rungs (leg). Figure 41 shows B_1 field distribution for 1.5 T – 4 T. From the result, we do not observe significant difference or improvement to implement 4-port excitation for 8-leg birdcage coil.

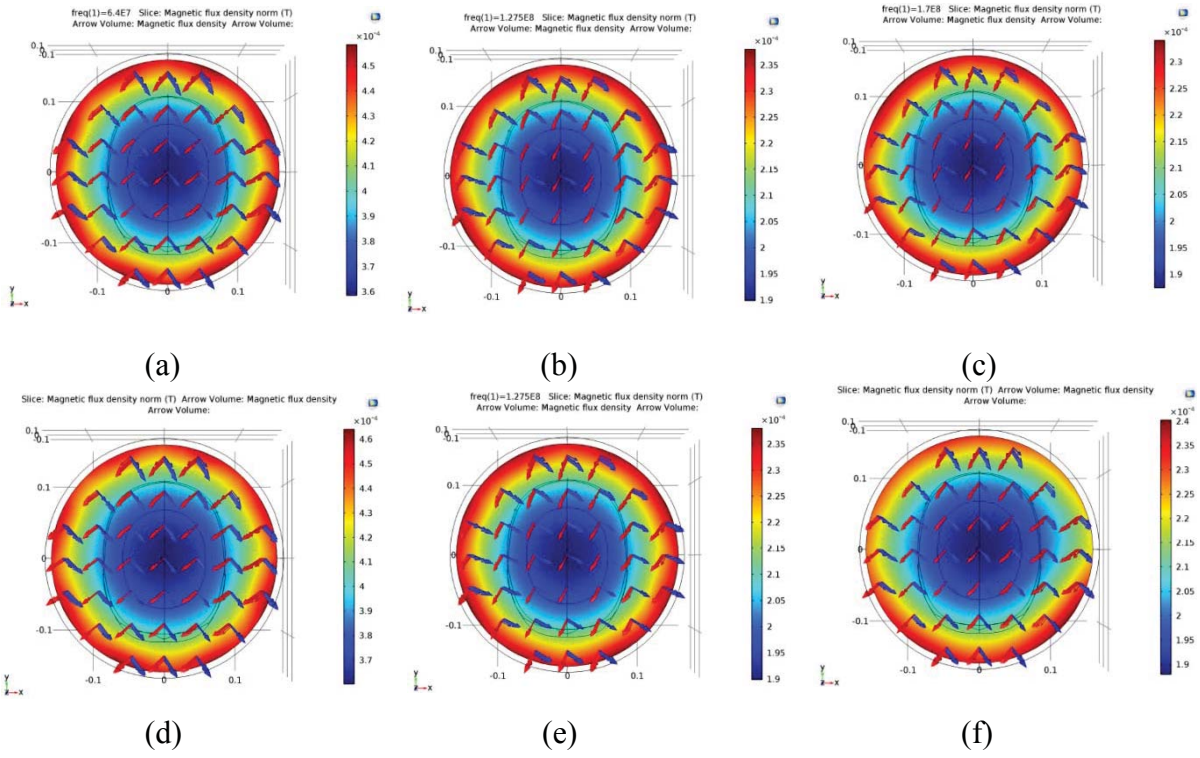

(a) (b) (c)

(d) (e) (f)

Figure 41: Magnetic flux norm (T) of unloaded coil: (a) 2-port at 64 MHz, (b) 2-port at 127.5 MHz, (c) 2-port at 170 MHz, (d) 4-port at 64 MHz, (e) 4-port at 127.5 at MHz, (f) 4-port at 170 MHz

CHAPTER 5

HIGH-PASS BIRDCAGE COIL MODELING AT 200 MHz

5.1 Capacitance Tuning

Although using low-pass birdcage coil gives uniform homogenous field (< 4 Tesla), as the Larmor frequency increases the uniformity of magnetic field starts to deteriorate, leading to high signal to noise ratio and high specific absorption rate (SAR) damaging tissue cells. Also, as seen from Figure 42, the coil self-resonates (0 pF) at 200 MHz and no capacitance value can be obtained for low-pass coil at high frequency. Therefore, high-pass birdcage coil is simulated at 200 MHz. Simulations are made for unloaded and shielded 12-leg high-pass birdcage coil with a diameter of 24 cm, a shield diameter of 44 cm and length of 15 cm at 200 MHz (~4.7T). In addition to using parametric sweep to determine optimum capacitance for each leg, Penn State Birdcage Builder application is used to validate our result [24, 25].

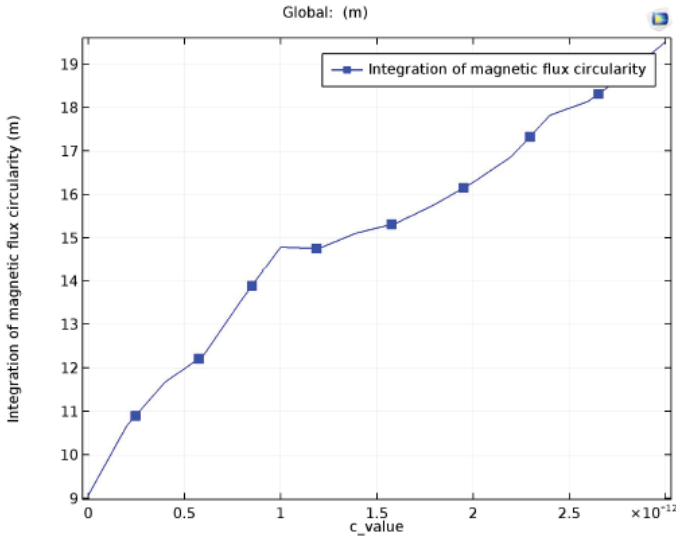

Figure 42: The axial ratio of the magnetic flux of the magnetic flux density around the head model at 200 MHz for low-pass coil

Figure 43 shows the user interface of Penn State Birdcage Builder. After we input the coil models and the desire frequency, an optimal capacitance is found to be 11.64 pF. For the setup of the coil model, the type of leg and end ring (ER) will determine the dimension of the coil. Since the model designed for this specific model is rectangular, we choose rectangular for both leg and end ring (ER). The next step is to input the coil radius, RF shield, the number of legs, type filters (low-pass, high-pass and band-pass) and the desired resonant frequency. In Figure 43 (b), the calculated capacitance value and current distribution in the legs are shown.

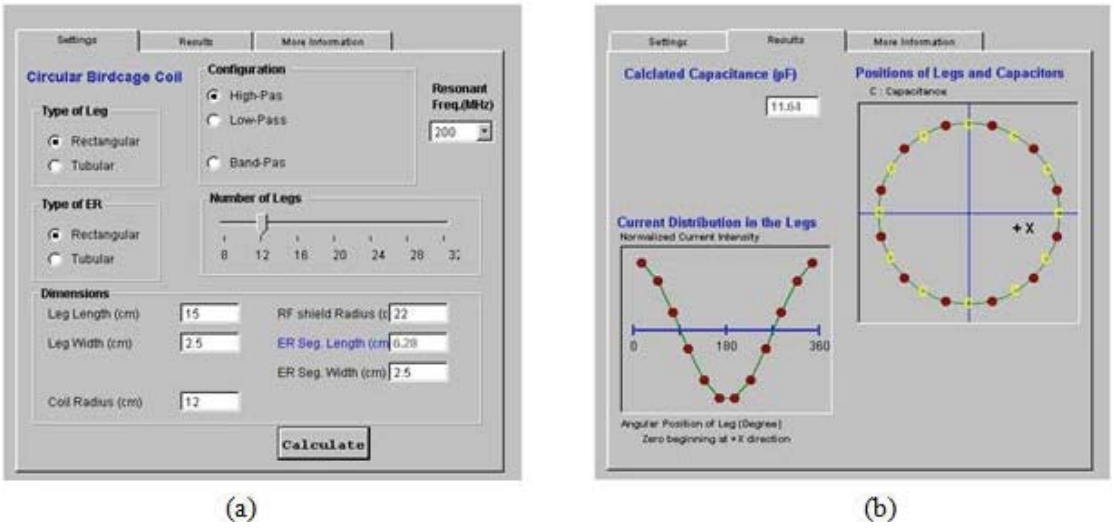

Figure 43: Birdcage Builder graphical user interface: (a) input parameter setup in the setting menu (b) optimum calculated capacitance and current distribution

5.2 COMSOL Multiphysics Simulation

Similar to low-pass birdcage coil, the geometry of the high-pass birdcage coil is built in the simulation environment as seen in Figures 44. All elements including rungs, end rings, lumped capacitors are modeled in the 2D as rectangular strips. After modeling the geometry, boundary conditions are applied. Rungs, end-rings, and RF shields are modeled using perfect electric conductor (PEC) boundary condition.

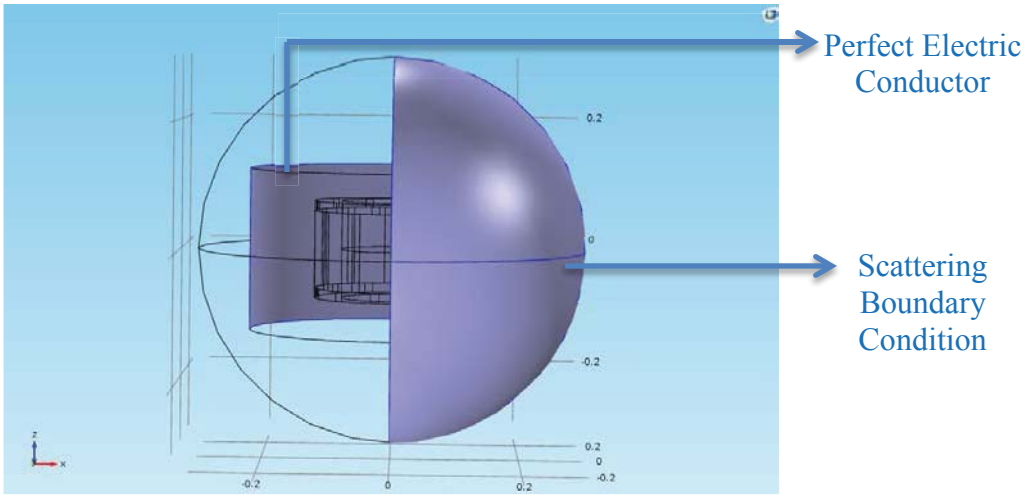

Figure 44: Geometric model of 12-leg shielded and unloaded high-pass birdcage coil

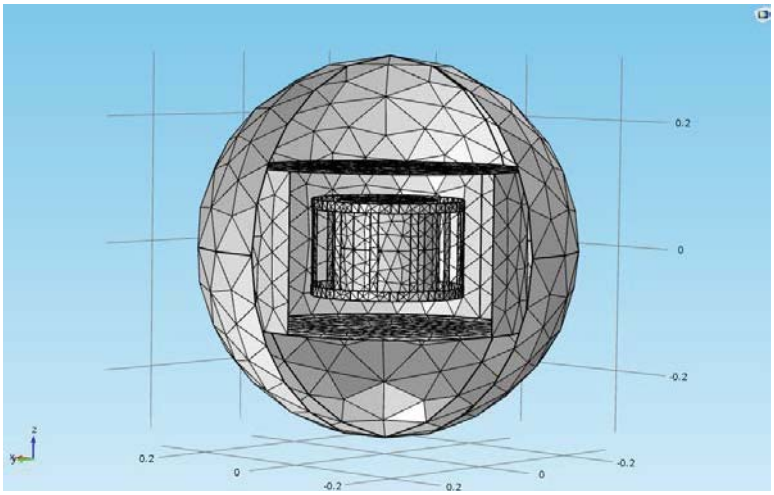

Figure 45: Mesh sturcture for high-pass birdcage coil without sphere phantom

Finer mesh is used to discretize the model as shown in Figure 45. The number of tetrahedral elements is found to be 33,407. The first simulation has been made for the empty 12-leg high-pass birdcage coil with a diameter of 24 cm, shield diameter of 44 cm, rung length of 15 cm, rung and end-ring width of 22.5 cm. In order to find optimum capacitance value, we use parametric sweep by ranging the capacitance values from 10 pF to 13 pF with a step capacitance of 0.2 pF for a given frequency value (200 MHz). Tuning the capacitor without the sphere model takes 2.1 GB memory with total run time of 304 sec.

From Figures 46 and 47, the optimum capacitance value to make the coil resonate at 200 MHz is found at 11.8 pF. This value is very close to the value that found from Penn state Birdcage Builder.

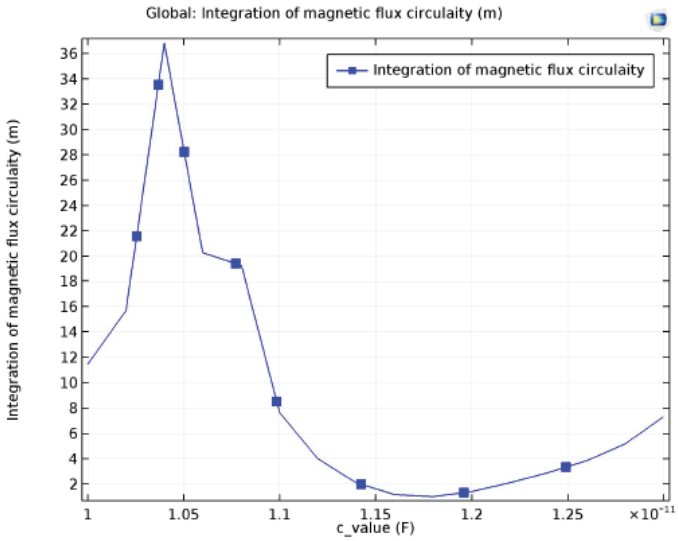

Figure 46: The axial ratio of the magnetic flux for coil only at 200 MHz

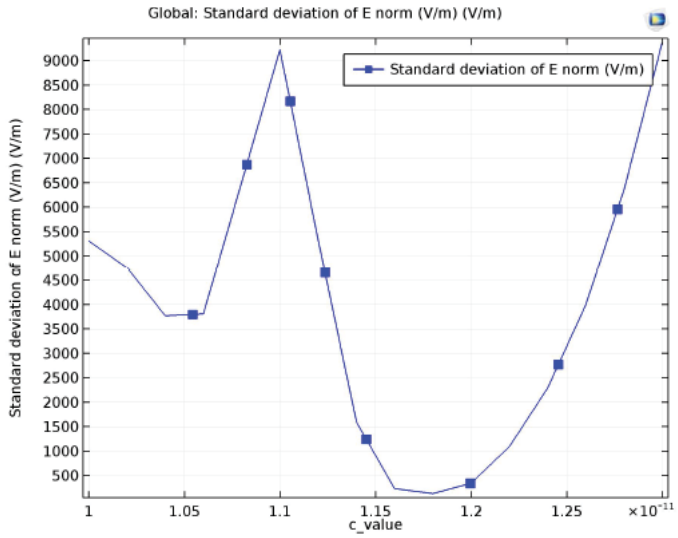

Figure 47: The standard deviation of the electric norm for coil only at 200 MHz

The first simulation is made for shielded and unloaded 12-leg high-pass birdcage coil. As can be shown from Figure 48, B_1 field is distributed uniformly along the coil. The orthogonality of the magnetic flux indicates the flux is rotating circularity.

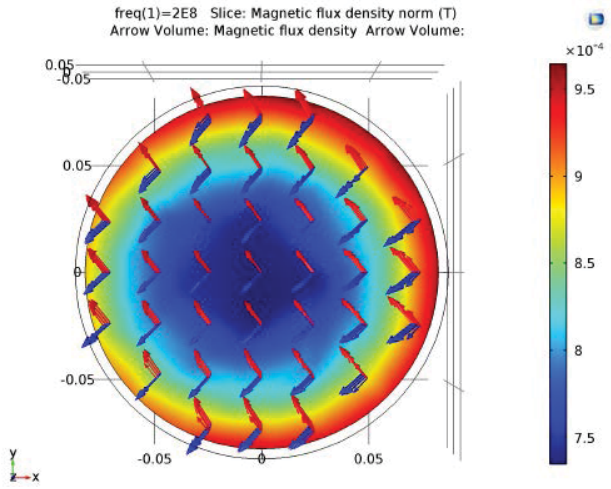

Figure 48: Magnetic flux density norm distribution with an arrow of the real (red) and imaginary (blue) part of the magnetic flux density for high-pass empty birdcage coil at 200 MHz

When the sphere phantom is placed, the capacitor can be further tuned for the loaded case to get a better result. Figure 49 shows the capacitor values for an empty and loaded case. From the plot, we can conclude no significant difference between the optimum capacitance values.

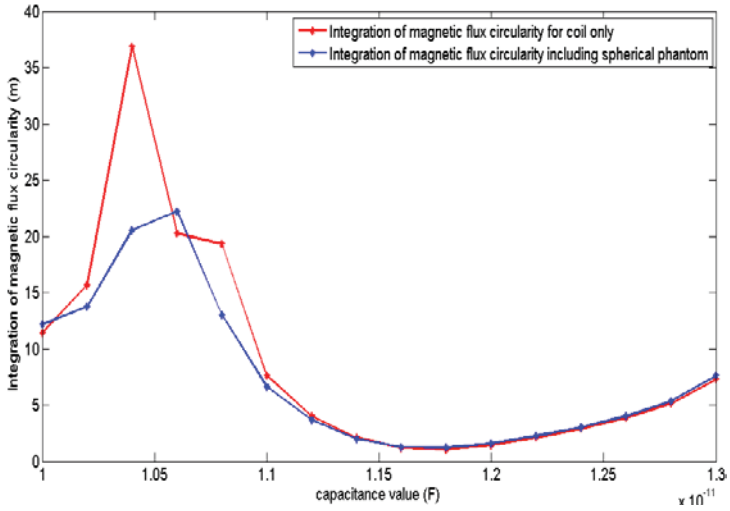

Figure 49: The integration of the axial ratio of the magnetic flux when loaded with spherical phantom and unloaded empty coil at 200 MHz

The second simulation is made for a loaded spherical phantom with a radius of 0.05 m. As seen from Figure 49, the optimal capacitance value to achieve homogeneity and circularity at 200 MHz is found to be11.8 pF. We use spherical phantom inside the coil with the following skin tissue parameters of σ = 0.44 S/m, $\mu_r = 1$ and ϵ_r = 42.8. The geometry of the model is shown in Figure 49. The total number of degrees of freedom for this case is 224,782 while using 1.73 GB memory size with total run time of 17 sec. From Figure 51, we can see the B_1 field is stronger at the center region compared to when there is no head object. The homogeneity deteriorates significantly due to the presence of the spherical phantom.

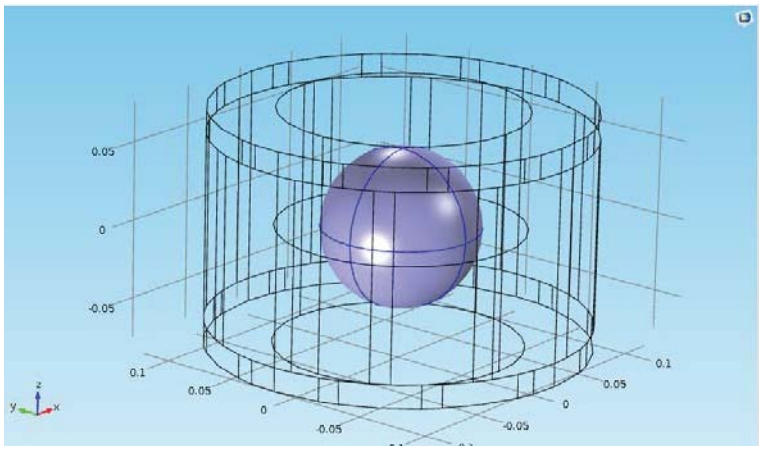

Figure 50: Geometric model of 12-leg high-pass birdcage coil with spherical phantom

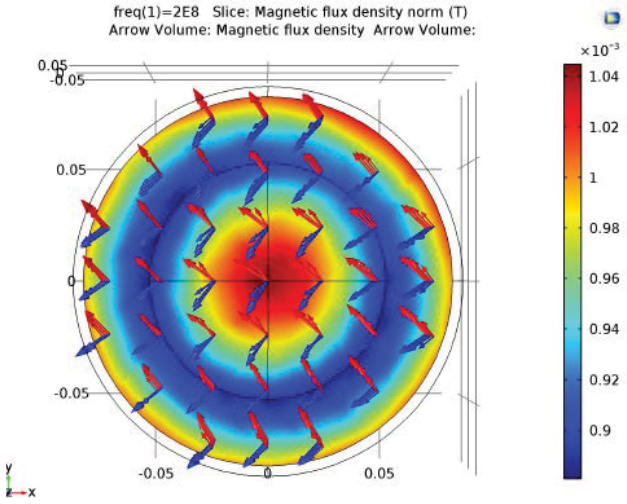

Figure 51: Magnetic field norm of loaded with spherical phantom at 200 MHz

In addition to the magnetic field, frequency domain analysis can also be used to calculate the SAR value using the formula given in Eq. (3.11), where σ and ρ of the brain tissue material properties given above are used at 200 MHz. From Figure 52, we observe that the SAR is low at the center but gets higher further close to the coil. The reason that SAR is low in the central region is due to the low electric field intensities as shown in Figure 53.

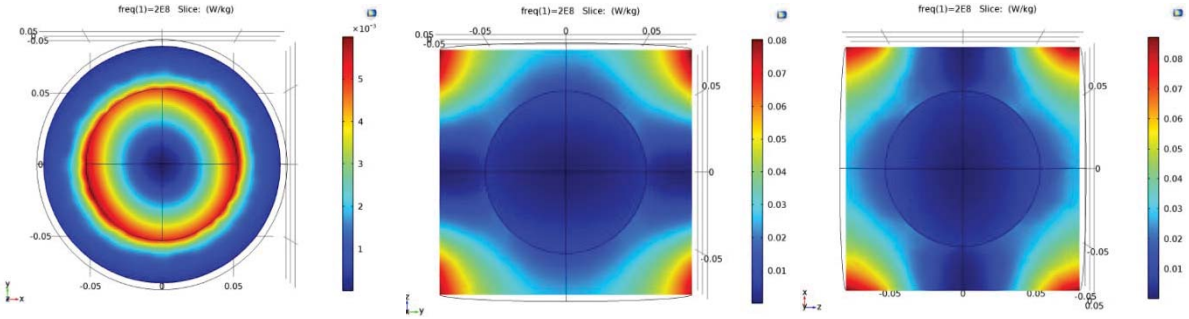

Figure 52: Sliced SAR distribution (a) axial (b) sagittal and (c) coronal slices of the human phantom at 200 MHz

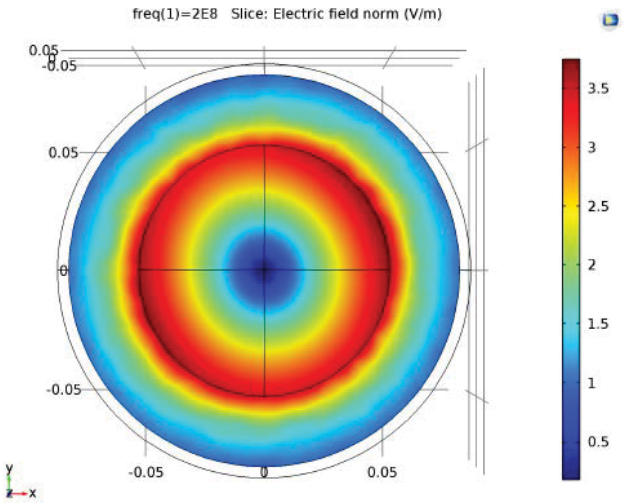

Figure 53: Electric field norm of loaded high-pass coil at 200 MHz

The material properties inside the birdcage coil dictate the homogeneity and distribution of B_1 field. As mentioned in section 3.6, the dielectric properties of materials are obtained from their measured complex relative permittivity. Figure 54 shows the magnetic field distribution inside the coil with spherical head phantom having different relative permittivity. B_1 field is high at the center as the relative permittivity

(ϵ_r) increases, at low ϵ_r we find that the field distribution is similar to empty birdcage coil having low B_1 field at center. Here σ is used as 0.1 S/m for all the cases.

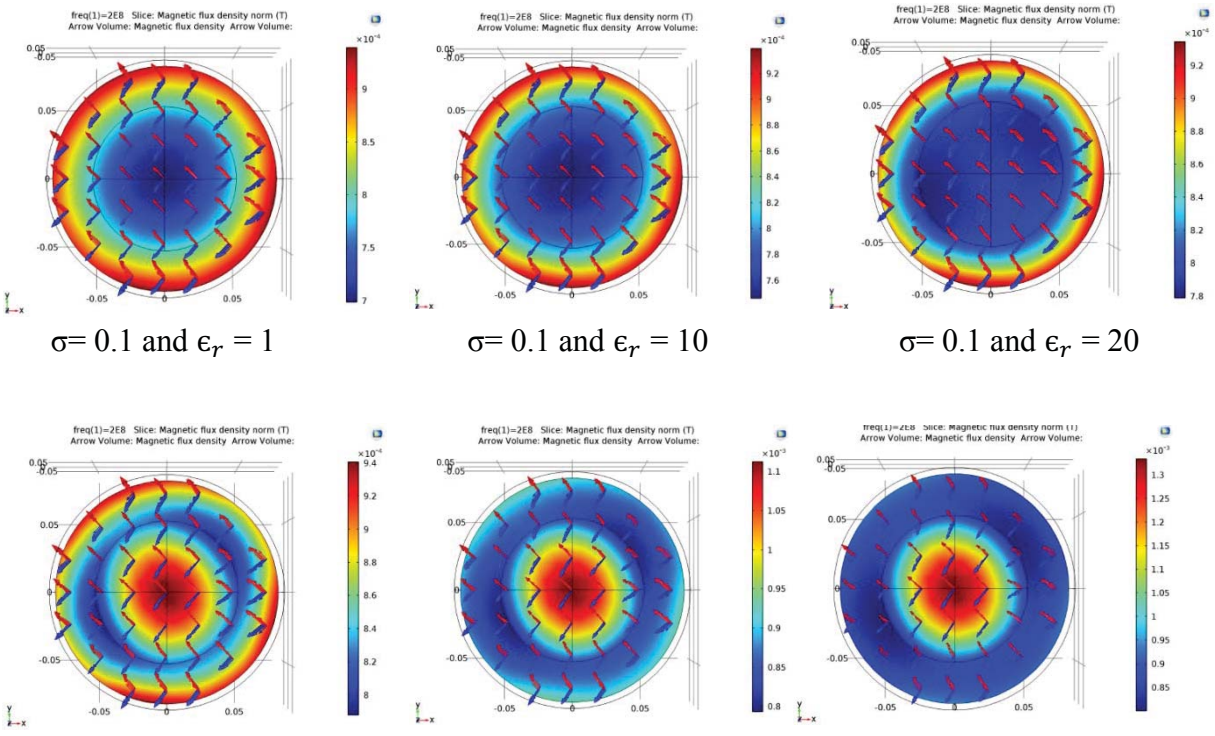

σ= 0.1 and ϵ_r = 1 σ= 0.1 and ϵ_r = 10 σ= 0.1 and ϵ_r = 20

σ= 0.1 and ϵ_r = 40 σ= 0.1 and ϵ_r = 60 σ= 0.1 and ϵ_r = 80

Figure 54: B_1 field norm of loaded with spherical phantom at 200 MHz for different relative permittivity

5.3 Convergence Study

As mentioned in Chapter 3, numerical methods have errors compared to their true solution of the PDE. Convergence study allows us to get close to the exact solution by refining mesh sizes. If the maximum element size is less than λ/6 = 0.038 m for the loaded birdcage coil, we can conclude the simulation result converges. Similarly, for the unloaded birdcage coil, the maximum element size has to be less than λ/6 = 0.025 m. From Table 7, only extra fine and extremely fine mesh sizes satisfy the requirement for the loaded birdcage coil while finer, extra fine, and extremely fine mesh sizes are used for the unloaded birdcage coil. Figure 55 shows the simulation result for unloaded coil for fine, extra fine and extremely fine mesh. We can see that the results are close to each

other. Figure 56 shows the results for the loaded the coil for three types of meshes. We can see that the result converges as the number of mesh increases.

Table 7: Number of elements and maximum element size for different types of meshes at 200 MHz

Frequency	Mesh type	Tetrahedral element (unloaded)	Tetrahedral element (loaded)	Maximum element size (m)
200 MHz	Finer	33,407	35,227	0.033
	Extra fine	89,788	93,665	0.021
	Extremely fine	433,221	440,270	0.018

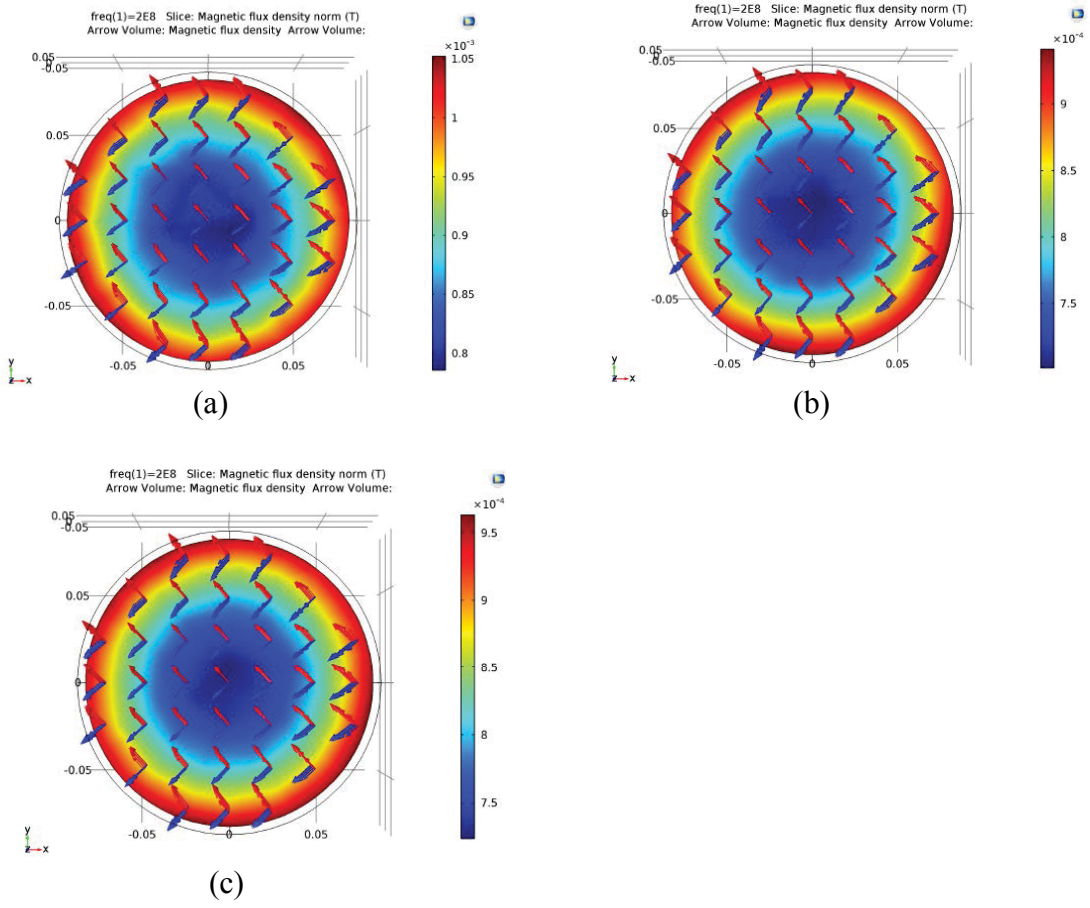

Figure 55: Magnetic flux density norm distribution with an arrow of the real (red) and imaginary (blue) part of the magnetic flux density for high-pass unloaded birdcage coil using (a) finer mesh, (b) extra fine, and (c) extremely fine mesh at 200 MHz

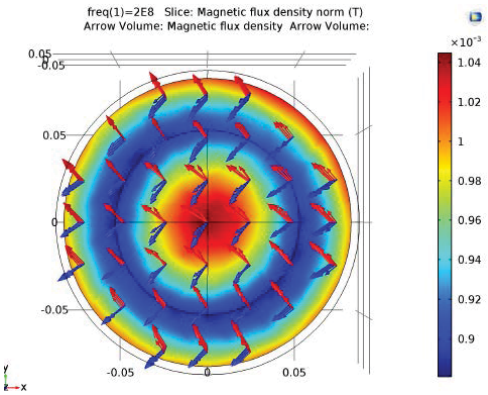

(a)

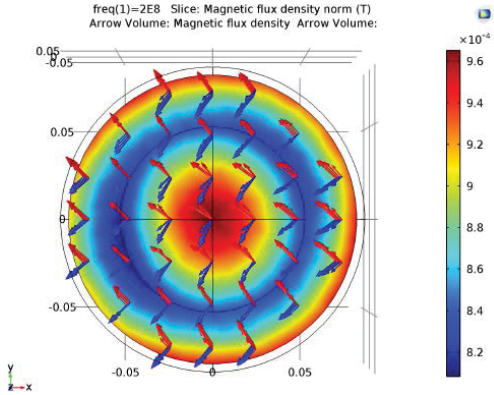

(b)

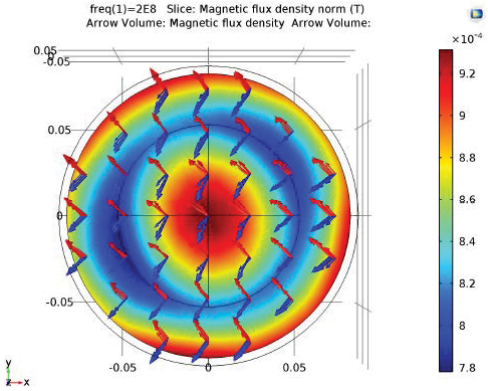

(c)

Figure 56: Magnetic flux density norm distribution with an arrow of the real (red) and imaginary (blue) part of the magnetic flux density for high-pass birdcage coil loaded with spherical phantom using (a) finer (b) extra fine and (c) extremely fine mesh at 200 MHz

CHAPTER 6

CONCLUSION AND FUTURE WORK

6.1 Conclusion

In this thesis, we analyzed RF birdcage coil using 3D FEM modeling from COMSOL Multiphysics for low-pass and high-pass birdcage coils. In order to effectively design a birdcage coil, capacitance tuning is necessary. Two methods are applied in this thesis to determine optimum capacitance value to obtain homogenous magnetic field distribution.

In designing the birdcage coil, lumped circuit element method is commonly used for low frequencies, where the coil dimension is smaller than the wavelength. However, as the frequency increases, the quasi-static approximation begins to fail when the wavelength is comparable with the coil dimension. Therefore, we used the 3D FEM to simulate the birdcage coil.

In the simulation process, frequency analysis is used to find the optimal capacitance value at the Larmor frequency. A parametric sweep is carried out for the capacitance of the coil. Lumped ports are used to provide quadrature excitation. We simulated two types of birdcage coils, low-pass and high-pass. For each type of coil, capacitors are placed accordingly to the type of coil to determine the resonant frequency and the uniformity of the field it produces. Scattering boundary conditions are used to avoid any electromagnetic wave reflection back to the coil. In addition, both the surface of the coil and shield around the coil are assigned as PEC boundary conditions.

In order to obtain both homogenous and circularly rotating B_1 field at the desired frequency, the capacitance is tuned using the parametric sweep. The circularity of the field is evaluated by estimating the axial ratio of the magnetic field around the phantom while the homogeneity of B_1 field is calculated using the standard deviation of the electric field around phantom. Furthermore, the analysis is performed to estimate SAR at the tissue level.

We are able to discretize the birdcage coil to get an accurate result by refining meshes. In order to obtain an accurate result, the maximum size of the mesh elements must be at least $\lambda/6$.

Additional software is used to validate our result to find optimum capacitance value. Birdcage Builder gives us results close to the values we obtained by finite element method using COMSOL Multiphysics.

6.2 Future Work

In the future, more results can be conducted by running simulations for ultra-high MRI systems ($\geq$ 7T). Since birdcage coil is limited, as the frequency gets larger, other types of coils must be used to get a homogenous magnetic field to accurately describe the interaction of electromagnetic waves with the human body.

REFERENCES

1. Medscape Multispecialty, "Understanding MRI," 2013. [Online]. Available: http://www.medscape.com/viewarticle/7809173. [Accessed 20 Jan 2016].
2. M. Lang, "Building a Birdcage Resonator for Magnetic Resonance Imaging Studies for CNS Disorders," University of Winnipeg, April 2011.
3. M. Elumalai, "Birdcage Coils for MRI-in Vivo Imaging of 25-Chlorine and 1-Hydrogen Nuclei," *Magnetic Resonance Imaging*, pp. 1-16, 2011.
4. Maxim Integrated, "Introduction to Magnetic Resonance Imaging," 2010. [Online]. Available: https://www.maximintegrated.com/en/appnotes/index.mvp/id/4681. [Accessed 29 Sep 2016].
5. S.S. Hidalgo-Tobon, "Theory of Gradient Coil Design Methods for Magnetic Resonance Imaging", *Concepts Magnetic Resonance*, pp. 223-242, 2001.
6. C. Chen, et al., "Quadrature Detection Coils-A Further √2 Improvement in Sensitivity," *Journal of Magnetic Resonance*, vol. 54, pp. 324-327, 1987.
7. M. C. Leifer, "Resonant Modes of the Birdcage Boil," *Journal of Magnetic Resonance*, vol. 124, no.1, pp. 51-60, Jan 1997.
8. J. Troop, "Theory of Birdcage Resonator," *Journal of Magnetic Resonance*, vol. 82, pp 51-62, March 1989.
9. F. W. Grover, "Inductance Calculations," *Dover Publications*, Mineola, NY, 2004.
10. Necip Gurler, "Finite Element Method Based Simulation, Design, and Resonant Mode Analysis of Radio Frequency Birdcage Coils Used in Magnetic Resonance Imaging," Bilkent University, March 2012.
11. J. Jin, "Electromagnetic Analysis and Design," *Analysis and Design of RF Coils*, pp. 138-202, 1999.
12. J. M. Jin, J Chen, W. C. Chew, H Gan, R. L. Magin and P. J. Dimbylow, "Computational of Electromagnetic Felds for High-Frequency Magnetic Imaging Resonance Application," *Phys. Med. Bio*., vol. 41, pp. 2719-2738, 1996.
13. C. E. Hayes, "The Development of the Birdcage Coil Resonator: A Historical Perspective," *NMR in Biomedicine*, vol. 22, pp. 908-918, 2009.

14. J. M. Jin, G. Shen, and T. Perkins, “On the Field Inhomogeneity of a Birdcage Boil,” *Magnetic Resonance in Medicine*, vol. 3, no.5, pp. 730-746, Oct 1998.
15. J. M. Jin and J. Chen, “On the SAR and Field Inhomogeneity of Birdcage Coils Loaded with the Human Head,” *Magnetic Resonance in Medicine*, vol. 38, no. 6, pp. 953-963, Dec 1997.
16. T. S. Ibrahim, R. Lee, B. A. Baertlein, Y. Yu and P. L. Robitaille, “Computational Analysis of the High-pass Birdcage Coil Resonator: Finite Difference Time Domain Simulations for High-field MRI,” *Magnetic Resonance Imaging*, pp. 835-843, May 2000.
17. A. Obi, “A Method of Moments Approach for the Design of RF COILS for MRI,” Worcester Polytechnic Institute, March 2008.
18. MRI Birdcage Coil, “COMSOL,” [online]. Available: http://www.comsol.com/model/download/233041/models.rf.mricoil.pdf. [Accessed 14 Oct 2015].
19. United States Food and Drug Administration, “Magnetic resonance diagnostic devices criteria for significant risk investigations,” [online]. Available http://www.fda.gov/RegulatoryInformation/Guidances/ucm073817.htm, 1998.
20. M. A. Stuchly and S. S. Stuchly, “Dielectric Properties of Biological Substances Tabulated,” *J. Microwave Power*, vol. 15, pp. 19-26, 1980.
21. D. Simunic, P. Wach, W. Renhart, and R. Stollberger, “Spatial Distribution of High-Frequency Electromagnetic Energy in Human Head During MRI: Numeric results and Measurements,” *IEEE Trans. Biomed. Eng*., Vol. 43, pp. 88-94, 1996.
22. C. Gabriel, S. Gabriel and E. Corthout, “The Dielectric Properties of Biological Tissues: I. Literature Survey, “Overview of Dielectric Properties: Terms and Definitions,” *Phys. Med. Bio*., vol. 41, pp. 2719-2249, April 1996.
23. K. Kalayeh, “Finite Element Convergence Studies of a Time-Dependent Test Problem Using COMSOL 5.1,” Tech. Rep. HPCF-2015-30, UMBC High Performance Computing Facility, University of Maryland, Baltimore county, 2015. Available: http://hpcf.umbc.edu.

24. Penn State College of Medicine, “Birdcage Builder,” [online]. Available: http://www.pennstatehershey.org/web/nmrlab/resources/software/javabirdcage/circular. [Accessed 5 March 2016].
25. C. Chin, C. Collins, S. Li, B. Dardzinski and M. Smith. “BirdcageBuilder: Design of Specified-Geometry Birdcage Coils with Desired Current Pattern and Resonant Frquency,” *Concepts in Magnetic Resonance*, pp. 156-163, 2002.